İSTANBUL TECHNICAL UNIVERSITY ★ INSTITUTE OF SCIENCE AND TECHNOLOGY

ANALYSIS AND IMAGE RECONSTRUCTION OF SYNTHETIC APERTURE RADAR RAW DATA

M.Sc. Thesis by

Cihan ERBAŞ, B.Sc.

504011208

Date of submission : 24 December 2002

Date of defence examination : 23 January 2003

Supervisor : Assistant Prof. Dr. Selçuk PAKER

Members of the Examining Committee : Associate Prof. Dr. Sedef KENT

Associate Prof. Dr. Nebiye MUSAOĞLU

JANUARY 2003

I would like to thank everyone who contributed to this study and I am grateful to my family who has always been with me.

January 2003 Cihan Erbaş

CONTENTS

ABBREVIATIONS

SAR	: Synthetic Aperture Radar
ERS	: European Remote Sensing Satellite
PRF	: Pulse Repetition Frequency
2 D FFT	: Two Dimensional Fast Fourier Transform
MKFFT	: Modified Kernel Fast Fourier Transform
ESA	: European Space Agency
NASA	: National Aeronautics and Space Administration
SIR	: Shuttle Imaging Radar
JERS	: Japanese Earth Resources Satellite
GOME	: Global Ozone Monitoring Experiment

FIGURE LIST

SYMBOL LIST

$A_{SC}(.)$: Acceleration vector for the spacecraft
c : Speed of light
f : Doppler frequency
f_{DC} : Doppler centroid
f_{DR} : Doppler frequency rate
$G(.)$: Transfer function of the system
$g(.)$: System impulse response
$H(.)$: Fourier transform of the recorded raw signal
h : Platform height
$h(.)$: Recorded raw signal
$k(.)$: Chirp waveform
L : Real aperture (antenna) length
λ : Wavelength for operation frequency
$\mu(.)$: Phase correction term
$p(.)$: Probability density function
R : Range
$R(.)$: Rayleigh distribution
R_F : Far range
R_N : Near range
R_r : Relative range vector
$R_{SC}(.)$: Position vector for the spacecraft
$R_T(.)$: Position vector for the target
r : Minimum range distance
r' : Azimuthal range coordinate
r_0 : Range to the image center
S : Swath width
t : Time variable
t_n : Time value for the n^{th} position of the real antenna
τ : Pulse duration
V_r : Relative velocity vector
$V_{SC}(.)$: Velocity vector for the spacecraft
$V_T(.)$: Velocity vector for the target
v : Speed of the sensor
$v(.)$: Function for range migration effect
v_r : Radial velocity
W : Real antenna width
w : Angular frequency
$w[.]$: Ground illumination function
w_e : Earth' s angular frequency
x : Azimuth coordinate of the target
x_n : n^{th} position of the real antenna
x_R : Location of the sensor

x_T : Location of the target
x' : Azimuthal azimuth coordinate
Δ_c : Range curvature
Δ_w : Range walk
Δf : Chirp bandwidth
Δr_g : Ground range resolution
Δr_s : Slant range resolution
Δx : Azimuth resolution
Θ : Look angle
Ψ : Beamwidth in azimuth direction
$\Psi(.)$: Phase term
Φ : Beamwidth in range direction
$\phi(.)$: Phase function
$\Gamma(.)$: Fourier transform of reflectivity pattern
$\gamma(.)$: Reflectivity pattern
α : Chirp rate
β : Squint angle
ζ : Fourier mate of azimuth samples
η : Fourier mate of range samples
σ^2 : Variance

YAPAY AÇIKLIKLI RADAR İŞLENMEMİŞ VERİLERİNİN İNCELENMESİ VE GÖRÜNTÜ OLUŞTURULMASI

ÖZET

Yapay açıklıklı radar (YAR) ile görüntülemenin kullanılabilirliği ilk olarak SEASAT uydusu kullanılarak elde edilen görüntüler ile gözlemlenmiştir. Elde edilen sonuçlar, uzaktan algılama konusunda öncülük etmiş ve birçok çalışma için temel oluşturmuştur. Yüksek çözünürlüklü görüntü elde etme özelliği yapay açıklıklı radarın jeolojik haritalandırma, tarım ürünü tanımlama, okyanus hareketlerini inceleme, sınıflandırma, afet belirleme, kutup buzlarını inceleme, çölleşmeyi gözlemleme gibi çeşitli uygulamalarda kullanılmasına imkan tanımıştır.

Yapay açıklıklı radar, yeryüzünün yüksek çözünürlüklü görüntüsünü, darbe işareti gönderip eşzamanlı yansıyan işaretleri toplayarak uzun bir anten sentezleme yöntemiyle elde eder. YAR aktif bir sensör olduğundan gönderdiği işaretleri kendisi oluşturur. Böylelikle pasif sensörlerdeki durumun aksine Güneş' ten bağımsız olarak her zaman görüntüleme gerçekleştirilebilir. Ayrıca elektromagnetik dalgaların bulutlardan geçebildiği mikrodalga bandında çalışılması hava şartlarından etkilenmeden görüntü alınmasını sağlar. YAR, bu önemli özellikleri nedeniyle giderek daha fazla kullanılmaktadır.

Yapay açıklıklı radar ile toplanan veriler etkin bir şekilde işlenmedikleri sürece anlamsızdırlar. Değişik işleme algoritmalar veriler üzerinde uygulanarak anlamlı görüntüler oluşturulmaktadır.

Bu çalışmada işlenmemiş uydu verileri çeşitli algoritmalarla işlenmiş ve görüntü oluşturulmuştur.İncelenen algoritmalar dar odaklama ve geniş odaklamadır. Her iki süreç için de sistemin transfer fonksiyonu elde edilmiş ve sonuçta göz önüne alınan coğrafi bölgelerin iki boyutlu görüntüleri oluşturulmuştur.

Çalışma boyunca ERS-2 platformunun işlenmemiş verisi kullanılmıştır. Örnek görüntüler İstanbul, Türkiye için verilmiştir.

ANALYSIS AND IMAGE RECONSTRUCTION OF SYNTHETIC APERTURE RADAR RAW DATA

SUMMARY

The feasibility of global mapping by spaceborne Synthetic Aperture Radar (SAR) systems was demonstrated by the successful SEASAT experiment. Many high quality images were obtained which constituted a basis for major developments in remote sensing. The feature of global mapping with high resolution made SAR a desirable imaging tool in many application areas such as geological mapping, crop identification, ocean circulation monitoring, land classification, disaster detection, polar ice monitoring, desertification assessment.

SAR produces high quality large scale images of the Earth surface via synthesizing a long antenna by transmitting pulses and coherently adding the successively reflected pulses to increase resolution in azimuth direction. Since SAR is an active sensor, that is it produces its own waveform and recieves backscattered signals, it is not dependent on sunlight providing day – and – night monitoring the Earth' s surface. In addition, SAR operates in microwave band which enables penetration of waves through clouds. Hence, monitoring of the Earth is cloud independent which is important for imaging regions that are constantly covered by clouds. Unique features of SAR makes it desirable and the number engineering projects on this area is incresing day by day.

Collected data by the SAR sensor is meaningless without proper and efficient processing. Images are produced by using raw data via different processing schemes.

In this study, raw data which are collected by spaceborne SAR sensors are processed by various algorithms. Examined algorithms are narrow focusing and wide focusing, namely. In both process operations, transfer function of the system is obtained. As a result, two – dimensional images of the illuminated surfaces are obtained.

During study, ERS-2 raw data is used. Sample images are given for Istanbul, Turkey.

1. INTRODUCTION

1.1. The Role of Synthetic Aperture Radar in Remote Sensing

In recent years, Synthetic Aperture Radar (SAR) techniques and its applications were much emphasized in the field of remote sensing. SAR sensors are being developed as a key mapping source day by day as their high quality imaging capability is realized and improved. While technological progresses are rapidly extended, both airborne and spaceborne SAR systems demonstrate their feasibility and more engineering projects on SAR are developed.

SAR is a microwave imaging system capable of producing high - resolution images from data collected over a large observation aperture by a small antenna. It synthesize a long antenna by transmitting pulsed signals and coherently adding the reflected signals successively to obtain high resolution in azimuth direction. The resolution in range direction is achieved by transmitting very short pulses or wide bandwidth pulses (chirp). Thus, SAR imaging sensor provides information about the surface by measuring and mapping the reflected energy in the microwave region. SAR has unique advantages which make it desirable for monitoring surfaces. It produces high - resolution images independent from sensor altitude via processing the returned signals. SAR has a day - and - night monitoring capability since it uses active sensors. Different from the passive operating mode, the active operating mode allows radar sensors to produce their own signals and receive returned echoes. Hence, they are independent from external sources such as sunlight. A cloud – independent nature exists because at microwave frequencies waves can penetrate clouds. As a result, a SAR operating in this frequency range is always able to image the illuminated surface under all weather conditions. SAR is mostly used for geological and forest mapping, crop identification, ocean circulation studies, land classification, polar ice monitoring, military applications, disaster detection, desertification assessment and planet mapping.

The wide varieties of potential applications of SAR imaging caused the development of the SEASAT satellite. The launch of the SEASAT satellite into the Earth orbit by NASA in June 1978, provided an opportunity to investigate the utility of SAR for environmental monitoring and ocean observation from space which was impossible before. During its mission period of three months, a large amount of imagery was obtained and it was shown that spaceborne SAR was an advantageous choice for global monitoring of the Earth. To obtain a better understanding of the spaceborne SAR remote sensing, a series of Shuttle Imaging Radar (SIR) flights, which include the 1981 SIR-A, 1984 SIR-B etc., was performed.

Recognizing the utilities of SAR, different countries developed their own spaceborne SAR sensors to obtain high – resolution images of the Earth for civilian applications. Russia launched in 1991 ALMAZ-1, Japan in 1992 JERS-1 and Canada in 1995 RADARSAT. European Union started ERS-1 and ERS-2 in 1991 and 1995, respectively. China has been developing a satellite called L-SAR. Its central electronics prototype was completed in 1997. In aircraft tests for demonstration, China ancient great wall hidden under dry soil was clearly discovered.

A very important feature of SAR application is on interplanetary issues. An interesting example is the Venus Radar Mapper called Magellan. The dense atmosphere of Venus was not a limitation for the SAR system. A global map of Venus with a resolution of 150 m was produced.

1.2. Scope of the Study

In this study strip mode SAR is of interest. In strip mode SAR, the antenna remains fixed with respect to the radar platform so that the antenna beam sweeps a strip on the ground. Successive wideband pulses are sent and backscattered signals which are called raw signal data are recorded. These data are then processed and a two – dimensional (2D) image of the surface reflectivity is produced.

Processing returned signals is an important task. Recorded raw data are visually meaningless since each backscattered signal is a coherent return of points within a beam. Thus, a kind of operation (focusing) must be performed to obtain high – resolution images of regions that are illuminated. A fully focused SAR image can be obtained by operating a filter which is related to the system impulse response on raw data. Hence, this application is dependent on the electrical (bandwidth,

frequency, pulse repetition etc.), cinematical (platform velocity) and geometrical (distance) parameters of the sensor.

The objective of this work is to analyze SAR raw data, reconstruct images via different processing algorithms using data that we have and to combine theory and practice on data processing issues. The method which is used to process SAR data is an inversion technique. As with most inverse problems, the extraction of the useful information from the received signal is mathematically ill – conditioned. To achieve sensible answers, some sort of regularization has to be done.

Our main goal is to characterize the reflectivity pattern of the illuminated surface. Reflectivity pattern can be expressed in terms of SAR raw data and impulse response of the system. Hence, impulse response of the system (in turn, transfer function) has to be evaluated as we already have the raw data. Transfer function is used as a matched filter to improve resolution in azimuth direction. It does not have an effect on resolution in range direction since range resolution is determined by pulse duration.

Two algorithms, namely narrow focusing and wide focusing, are examined for boresight geometry. Results achieved are satisfying; however, limitations of the algorithms cause imperfections over the images. Neglections such as earth rotation and approximations such as stop – start aproximation, which constitutes that a second pulse is transmitted after reception of the first echo related to the first transmitted pulse, are made, but these do not affect results vitally. Earth curvature is not considered as well. As a result, our system includes a flat earth with stationary targets.

With the approach used in our study, we can choose a certain amount of data set and operate on that chosen part without being have to process the whole data. It provides important advantages such as ability to focus on smaller portions of the whole geographical region which is handled. Thus, we do not need to process on raw data sections which are not of interest. This point of view terminates time consuming computer operations and computer memory problem. Moreover, used algorithms such as narrow focusing propose a high precision focus on a certain part of the images; it is not meaningful to operate on whole data to view a smaller fully focused area.

All calculations are operated on ERS–2 raw data. Obtained images are for the region Istanbul, Turkey. Fortran programming language is used to perform calculations and MATLAB is used for the plots.

1.3. Previous Studies on SAR Processing

The utilities of SAR are investigated and it is found to be useful in many geological issues. Wide application areas of SAR imaging cause major improvements on processing schemes. Different studies from different points of view on raw data processing are performed; processing algorithms which focus on different system parameters in order to increase azimuth resolution are developed. Franceschetti, Lanari and Marzouk [1] propose a method called modified kernel technique which investigates and compansates the space variance of the SAR transfer function in frequency domain. Space variance compansation is based on the use of a nonstandard Fourier Transform called Modified Kernel Fast Fourier Transform (MKFFT) in range direction. Two dimensional raw data spectrum is evaluated on a deformed grid instead of a conventional grid since space variance of the transfer function causes a grid deformation for transfer function as well. After a two – dimensional filter operation reflectivity spectrum grid distortion is removed. As a result, a fully focused image is obtained via modified kernel method compared with standard Fourier Transform (i.e. neglecting space variant part of the transfer function).

Another focusing method which is called hybrid digital correlation algorithm is suggested by Wu, Liu and Jin [2]. In this method, system impulse response (i.e. signal backscattered from a point target) is expressed as a convolution of two responses, namely range response and azimuth response. Azimuth response is processed in frequency domain and range response is considered in time domain. Hence, a hybrid data processing approach is performed. Simulation results for SEASAT SAR data is presented.

Prati and Rocca [3] develops a focusing technique for the time – varying Doppler centroid case. Due to platform instabilities, Doppler centroid changes accordingly during the platform motion. It also shows rapid linear variations with range. Variation of Doppler centroid causes a degradation in data spectrum. The technique is based on the reconstruction of the correct data spectrum from the deformed one. The method is applied on SIR-C SAR data and results are obtained.

Curlander, Wu, Li et. al. [4] gives two ' automatic ' techniques to estimate spaceborne SAR Doppler parameters by using only radar backscattered signal. As will be shown in the next sections, the expected phase history of a SAR system is approximated by two Doppler parameters, which are referred to the Doppler centroid and Doppler frequency rate. These quantities can be determined when all system data are precisely known. However, for the cases when accurate data are not available to the processor, automatic techniques which use solely coherent radar return for the estimation of Doppler parameters must be employed. Automatic estimations for Doppler centroid and Doppler frequency rate are called clutterlock and autofocus respectively. For clutterlock, Curlander proposes a method based on obtaining azimuth frequency specta for different segments of raw data to be processed. Raw data are divided into portions in azimuth direction. For each segment, Doppler centroid is evaluated and variation of Doppler centroid as a function of range is determined. For autofocus, he uses multiple – look and multiple – image approach. It is known that errors in Doppler frequency rate causes blurring (defocusing) in images. For a point target, full synthetic aperture length is divided into equal segments, obtained images are averaged and for a correct Doppler frequency rate these images overlay. However, an incorrect Doppler frequency rate results in multiple images. Proposed method relates location error of images and error in Doppler frequency rate and obtains the actual Doppler frequency rate value.

2. SAR THEORY AND RAW DATA PROCESSING

2.1. Introduction

In this section, we are concerned with SAR imaging principle and processing ERS–2 (European Remote Sensing Satellite) spaceborne SAR raw data via two algorithms. We will process images to the fullest resolution and be working on continuous strip – mapping spaceborne SAR.

We will first briefly review the basic principles of radar imaging, advantages of SAR imaging over real aperture radars. Then we will examine narrow focus and wide focus algorithms to process raw data that we have and reconstruct images. An important point of view is that we do not have to process all the raw data. With our approach, we are able to process a chosen region in raw data set and operate on that area. This is quite advantageous since it provides time efficiency and ability to focus on desired geographical regions. Also in narrow focusing case, as will be explained in the following sections, only a certain part of the image is fully focused. Hence, processing all raw data would not be logical to view only a small well – focused region. Moreover, computer memory problem is generally overcome via working on defined smaller raw data sets.

2.2. Principles of SAR Imaging

2.2.1. Basic Concepts

Before exploring SAR theory, it is necessary to define some basic definitions related to the subject which are important parameters for all steps. Moreover, properties of the chirp pulse (i.e. linear frequency modulated pulse) which is the transmitted waveform for most SAR systems must be considered.

Range: Distance between sensor and target

Azimuth: Direction of SAR sensor velocity vector

Range and azimuth configuration are given in Figure 2.1. Note that range distance in this figure is the minimum range distance in boresight geometry. At each step of the sensor, range distance changes accordingly. This condition is also given in the next sections.

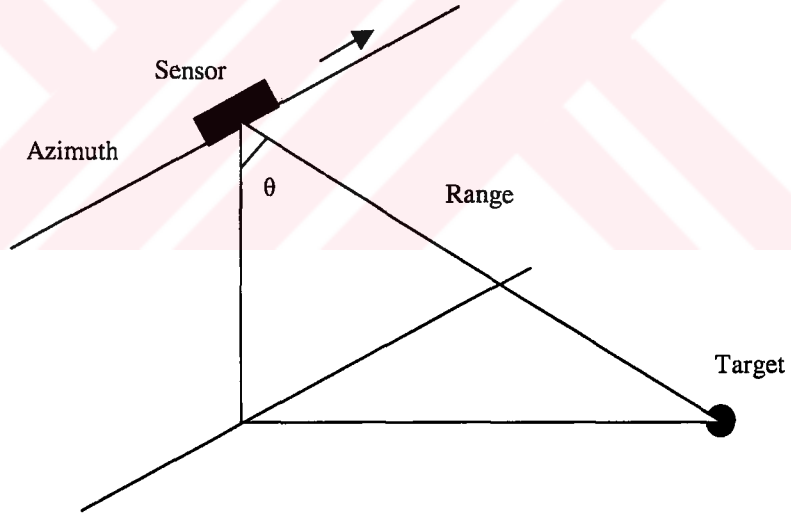

. Figure 2.1. System configuration for boresight geometry

Real Aperture (L): Length of the antenna of the sensor in azimuth direction

Synthetic Aperture: Length of total distance by the sensor during collection of data. A very large antenna is synthesized by moving along a reference path a real one of limited dimension. Definition of synthetic aperture is given in Figure 2.2 graphically.

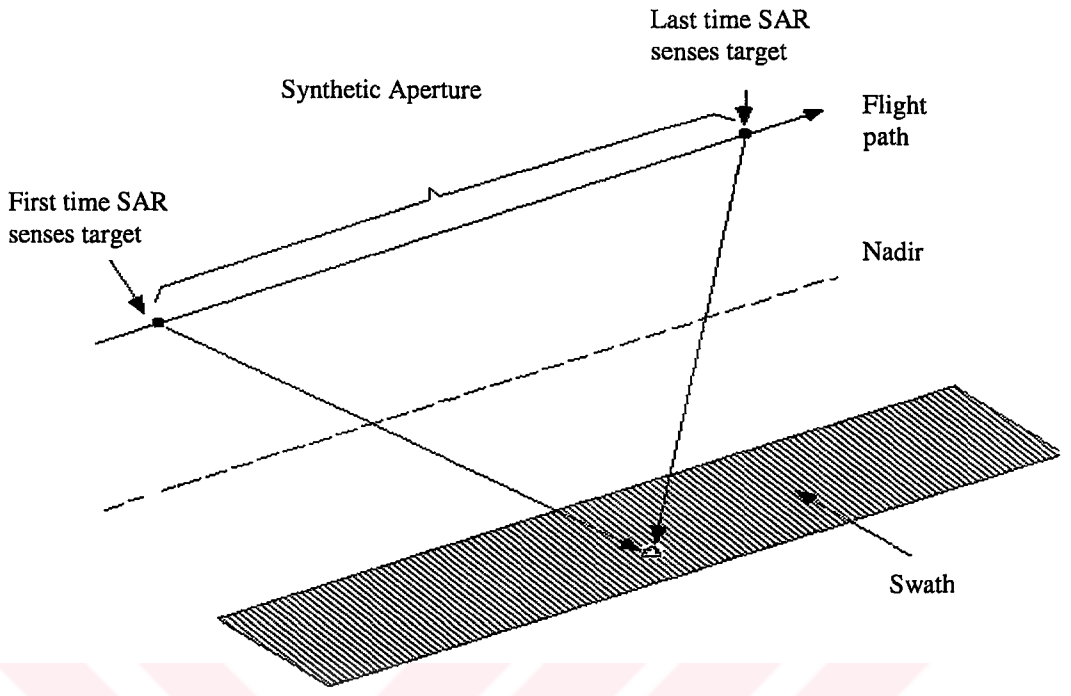

Figure 2.2. Synthetic aperture definition

Resolution: Resolution is defined separately for range and azimuth directions. Resolution in (ground) range is the minimum range separation of two points that can be distinguished by the system. Illustration for range resolution Δr_g can be seen in Figure 2.3. In that figure θ is the look angle, h is the platform height, Φ is the beamwidth in range direction, R_N and R_F are near and far ranges respectively, α is the angle between near range and normal and Δr_s is the resolution in slant range.

$$\Delta r_s = \frac{c.\tau}{2} \tag{2.1}$$

where c is the speed of light and τ is the transmitted pulse width.

$$\Delta r_g = \frac{\Delta r_s}{\sin\alpha} = \frac{c.\tau}{2.\sin\alpha} \tag{2.2}$$

If the bandwidth of the pulse (Δf) is approximated by $\Delta f \approx 1/\tau$ [1], we have

$$\Delta r \approx \frac{c}{2.\Delta f.\sin\alpha} \tag{2.3}$$

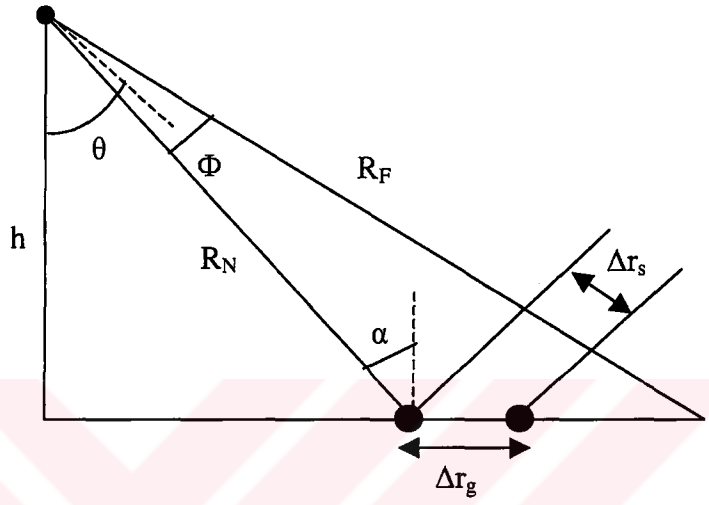

Figure 2.3. Geometry for range resolution expressions

An important point is that range resolution is determined by system characteristics and cannot be improved by processing operations.

Azimuth resolution for a real aperture radar (Δx) is the distance in azimuth dimension measured between the half power (-3 dB) points of the power response for a point target since two targets separated by this distance can be distinguished as two targets. This condition is given in Figure 2.4.

Azimuth resolution of a real aperture radar is the azimuth distance at some range R, multiplied by the beamwidth in azimuth direction as depicted in Figure 2.5. Hence, azimuth resolution (Δx) can be expressed as;

$$\Delta x = R.beamwidth \tag{2.4}$$

$$\Delta x = \frac{\lambda.R}{L} \tag{2.5}$$

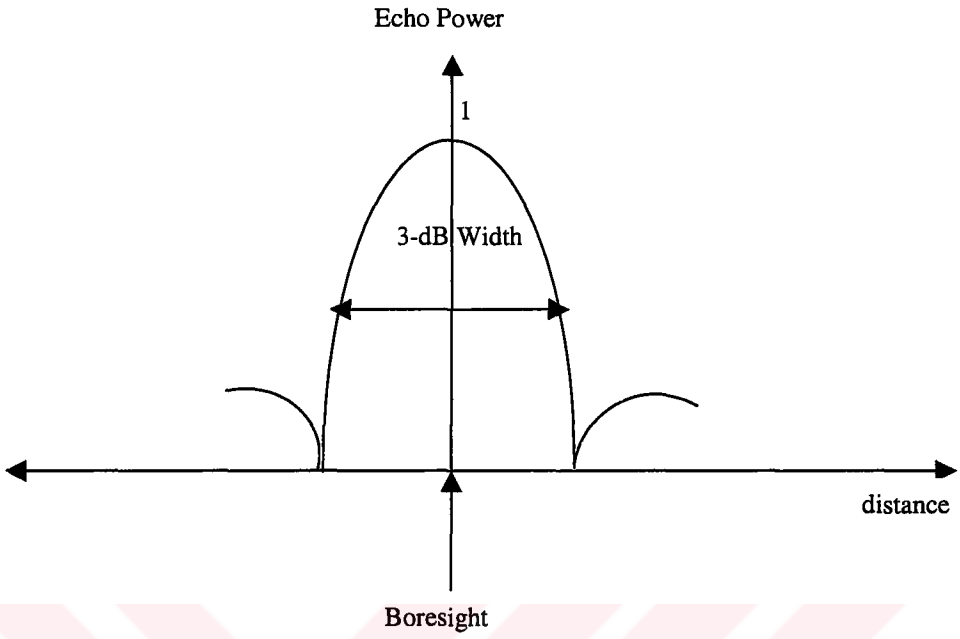

Figure 2.4. Illustration for azimuth resolution

where λ is wavelength for operation frequency and L is the length of the antenna in azimuth direction.

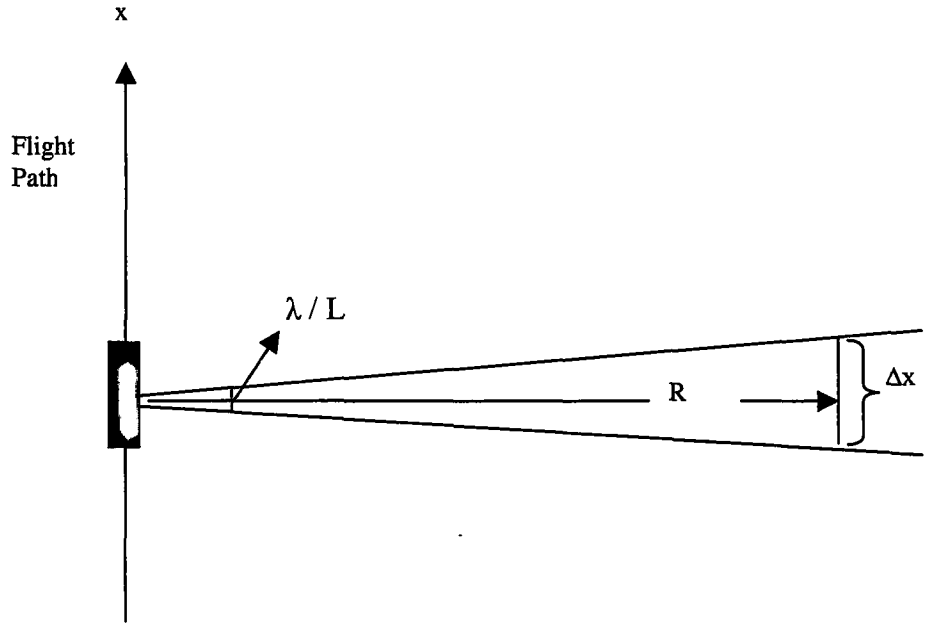

Figure 2.5. Azimuth resolution definition

Azimuth resolution has a high dependence on range. To have an idea of the achievable azimuth resolutions let us apply Equation 2.5 to ERS–2 sensor parameters; the azimuth resolution for a 850000 m range (around midswath) is 4.25 km, which is not acceptable for most applications. To improve azimuth resolution we must reduce wavelength of the operation frequency and / or increase antenna dimension; in the microwave region, apertures of many hundreds of meters to many kilometers are required to achieve high resolution of tens of meters or less. The former is constrained by the system characteristics. The latter is not an easy task, unless we implement the synthetic aperture (antenna) concept which is given above. For synthetic aperture radar (SAR), azimuth resolution is [2];

$$\Delta x = \frac{L}{2} \tag{2.6}$$

Azimuth resolution is not dependent on range; this dramatic resolution improvement is achieved via focusing (processing) procedure which is explained in the latter parts. It is not surprising to realize that in synthetic aperture radar, azimuth resolution is better for small antenna lengths and in real aperture radar, azimuth resolution is better for large antenna lengths as given in Equation 2.5, because as the antenna length decreases, synthetic aperture length for a point target (i.e. λ.R / L) increases. When the synthetic aperture is larger, it is possible to obtain more samples for the target, increasing the azimuth resolution. Resolution expression in Equation 2.6 is the maximum achievable value, in practice it is not fulfilled in practice since all focusing algorithms have limitations.

It is useful to investigate the pulsed signals which are used in SAR systems. To improve resolution in range direction either very short or large bandwidth pulses are used as expressed in range resolution equations. A large bandwidh pulse is the linear frequency modulated (FM) pulse. It is called chirp pulse in analogy to bird sounds. In complex notation a chirp is defined as;

$$k(t) = \exp\left[j\left(wt + \frac{\alpha t^2}{2} \right) \right] . rect\left[\frac{t}{\tau} \right] \quad , \qquad -\frac{\tau}{2} \le t \le \frac{\tau}{2} \tag{2.7}$$

Taking its real part;

$$k(t) = \cos\left(wt + \frac{\alpha t^2}{2} \right) . rect\left[\frac{t}{\tau} \right] \quad , \qquad -\frac{\tau}{2} \le t \le \frac{\tau}{2} \tag{2.8}$$

where w = 2.π.f is the angular frequency with f is the carrier frequency, and α is the chirp rate depicted as;

$$\alpha = \frac{2\pi.\Delta f}{\tau} \tag{2.9}$$

In our system, w = 3.297×10^{10} rad / sec and α = 26.32×10^{11} rad / sec^2. Illustration of the chirp pulse is given in Figure 2.6.

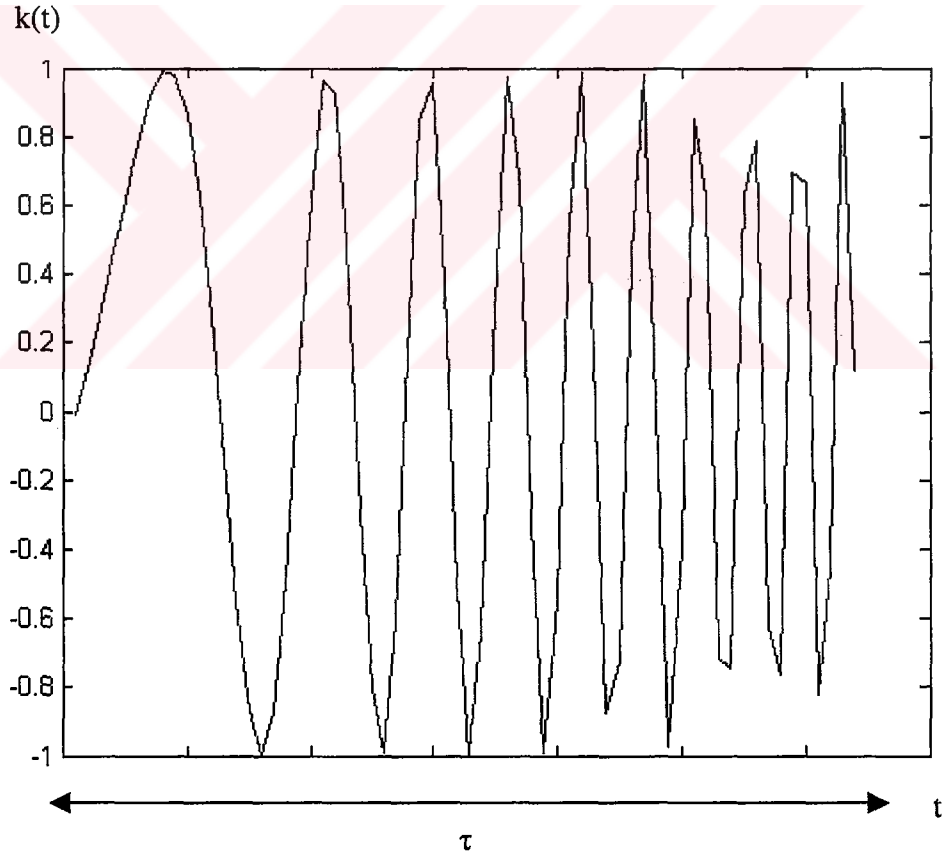

Figure 2.6. Chirp waveform (arbitrary units)

Note that chirp waveform increases its frequency linearly in time. Instantaneous angular frequency is evaluated as (see Appendix B);

$$w_{inst}(t) = w + \alpha.t \tag{2.10}$$

Variation of instantaneous angular frequency versus time is shown in Figure 2.7.

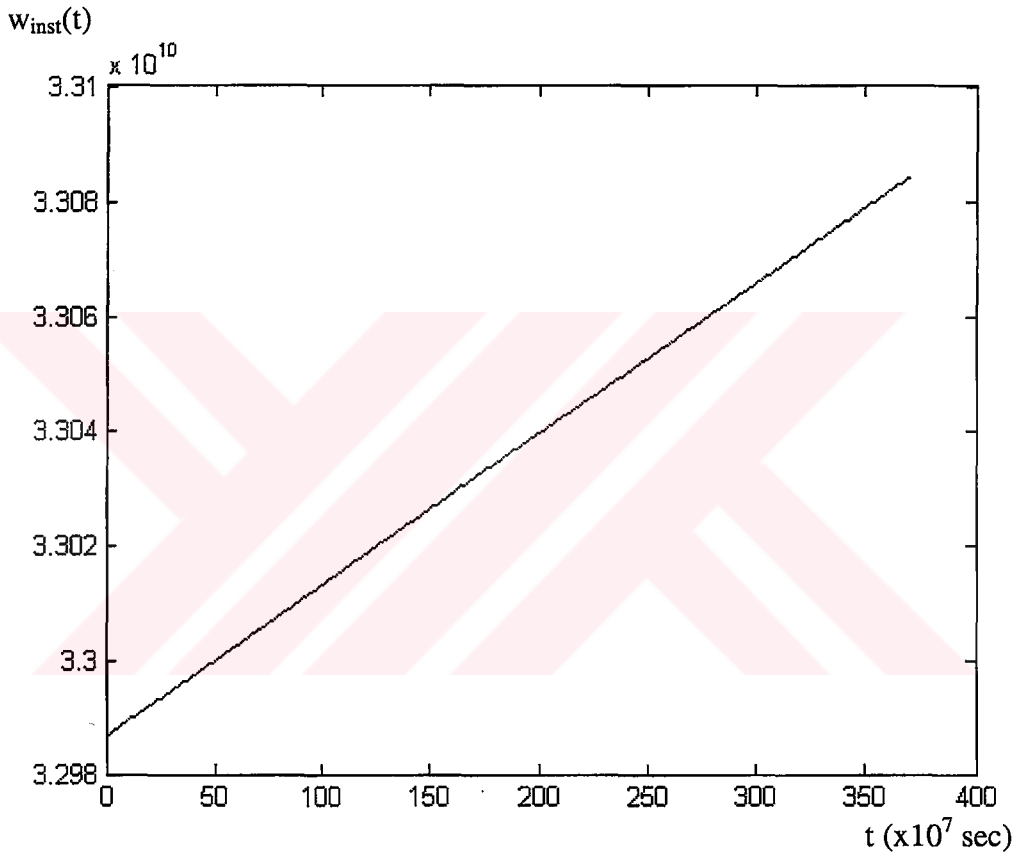

Figure 2.7. Variation of instantaneous angular frequency of the chirp pulse

2.2.2. SAR Operation Modes

There are basically three operating modes of a SAR system: Strip mode, scan mode and spot mode which are pictured in Figure 2.9 , Figure 2.10 and Figure 2.11, respectively.

The most popular and well- known is the strip mode. In this case, the radar antenna points along a fixed direction with respect to the flight platform path and the antenna footprint covers a strip on the illuminated surface as the platform moves and the system operates. The strip SAR image is limited in the range but not limited in azimuth direction.

The strip mode involves two imaging geometries. The most conventional one is referred to as ' boresight ' (as mentioned earlier), with the antenna beam pointing in the plane perpendicular to the flight direction. The other geometry is the ' squinted ' one, with the antenna making a point angle, referred to as squint angle with respect to the boresight direction which is shown in Figure 2.8. The squint angle can be a desired system characteristic or can be due to undesired motions of the platform. The squint angle can reach some tens of degrees.

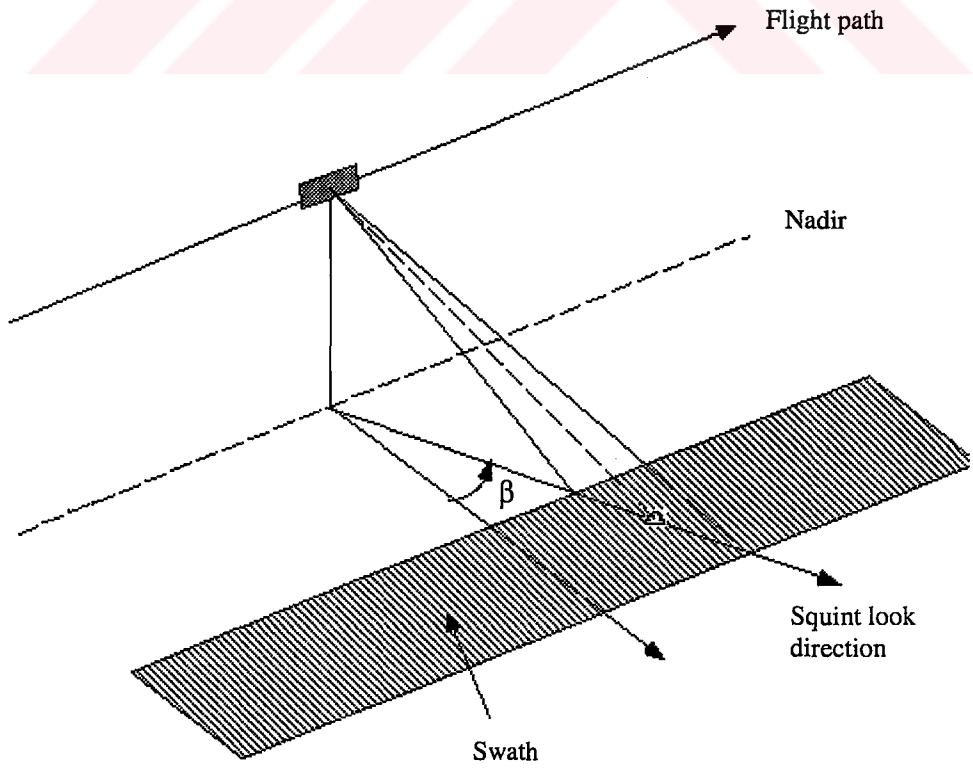

Figure 2.8 Squint angle illustration

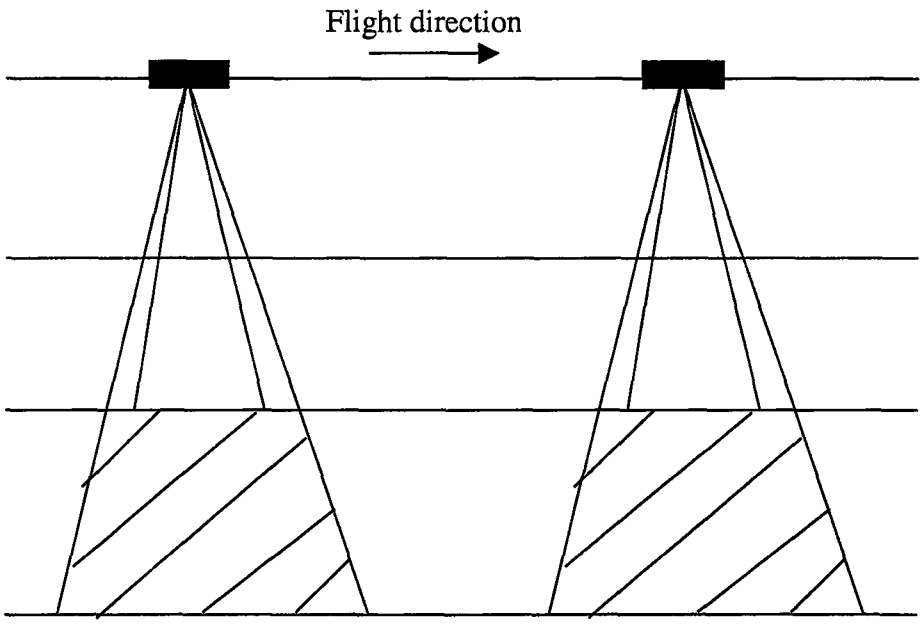

Figure 2.9. Strip SAR operation mode

The scan mode allows an increase in the range swath dimension. This is achieved by periodically stepping the antenna beam to neighbouring subswaths (in the range direction). In this case the radar is continuously on, but only portions of the full synthetic aperture length are available for each target in a subswath. This causes a degradation of the achievable azimuth resolution with respect to the strip mode. Hence, the range swath dimension increases at the expense of azimuth resolution.

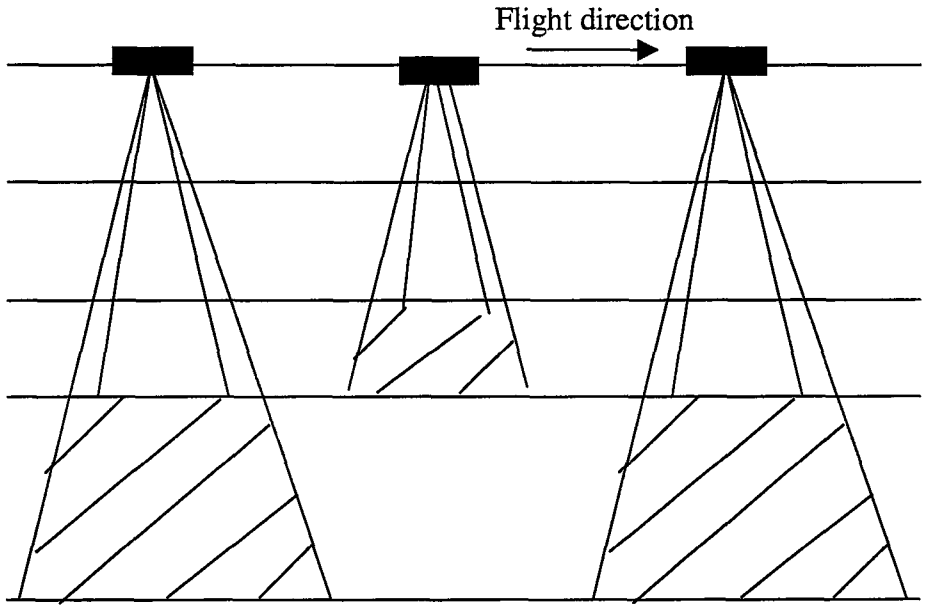

Figure 2.10. Scan SAR operation mode

The spot mode has a different approach. The radar antenna is steered during the overall acquisition time to illuminate the same area. The available synthetic aperture length can be increased with respect to the strip mode, thus improving azimuth resolution this gain is traded off by loss of coverage due to the illumination of a limited area along the sensor flight path.

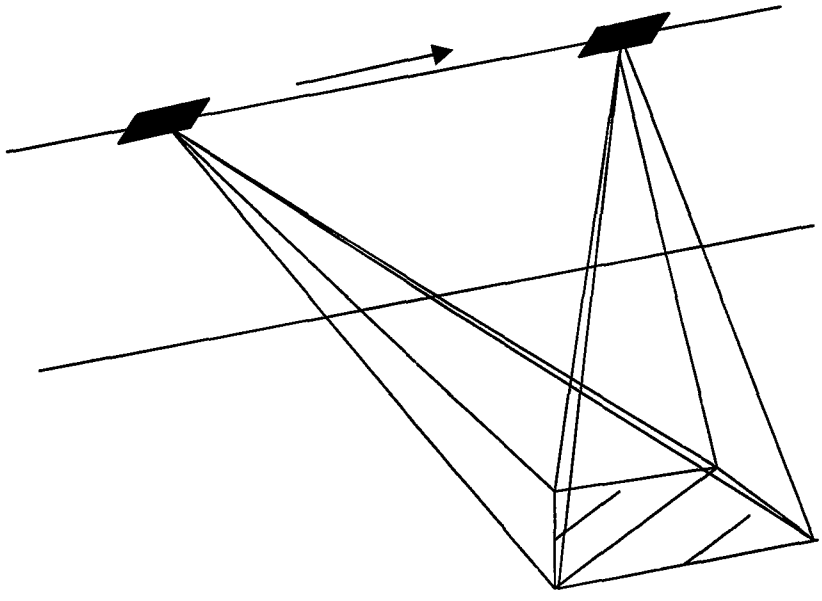

Figure 2.11. Spot SAR operation mode

2.2.3. SAR Theory

The technique of using coherent radar pulses to increase azimuth resolution was invented in 1950s. It was realized that the Doppler frequency shifts of stationary targets with respect to the moving radar sensor could be used to distinguish the different targets that are at the same range distance from the radar.

Consider a radar sensor moving along a straight line as shown in Figure 2.12. It carries a transmitter that sends out radar waves of wavelength λ, and an antenna that receives the backscattered waves. Suppose it has just transmitted a pulse of radar waves. A target or scatterer that is behind the sensor, for example point C, appears to be moving away from the aircraft. Due to the Doppler effect, it will return a signal that is of lower frequency than the transmitted radar pulse. In contrast, a target that is in front of the sensor, for example point A, will return a signal of higher frequency than that transmitted. Signals from points that are in boresight (i.e. the lines joining these points to the radar are perpendicular to the flight direction), for example point B, will not experience any Doppler shifts.

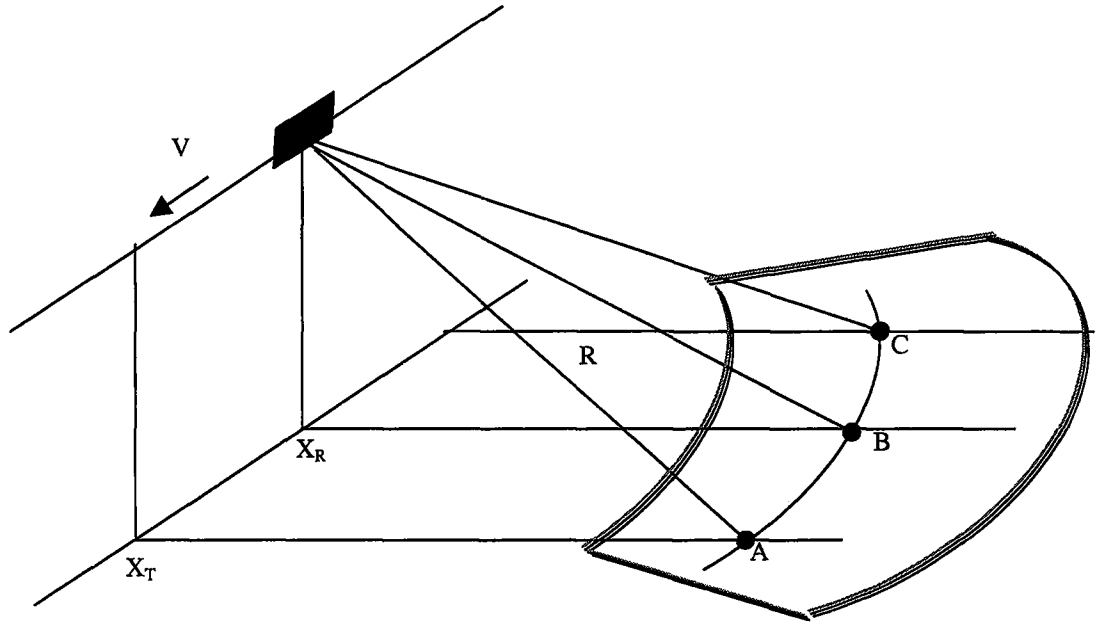

Figure 2.12. Illustration for Doppler frequency shift

In the figure, points A, B and C are located at the same range distance R from the radar and so the antenna will simultaneously receive the combined signals of these points (and all other points in the curve). Obviously, it will not be possible to distinguish the points A, B and C from one another, based on only one range measurement. The solution is to combine multiple coherent returns.

Referring to Figure 2.12, point A is just entering the area illuminated by a radar pulse (illuminated area is shown within the shaded borders). Suppose the speed of the aircraft is V. Then at this instant, the velocity component of this point relative to the aircraft, along the line joining it to the radar antenna is given by;

$$v_r = \frac{V.(x_R - x_T)}{R} \tag{2.11}$$

x_T and x_R being respectively, the target and radar location along the line of flight ($x_T > x_R$). Due to the Doppler effect, the frequency of the signal from target A differs from that of the transmitted pulse by the following amount:

$$f(x_R) = -\frac{2.v_r}{\lambda} \tag{2.12}$$

$$f(x_R) = -\frac{2.V.(x_R - x_T)}{\lambda.R} \tag{2.13}$$

This change in radar frequency is called ' Doppler frequency '. It is clear that the Doppler frequency changes with antenna position x_R since x_T is fixed.

In the synthetic aperture technique, the Doppler information of the backscattered wave is used simultanously with the time delay information to generate a high resolution image of the surface being illuminated by the radar. Points equidistant from the radar are located on concentric spheres as given in Figure 2.13. The backscattered waves from targets along a certain circle will have the same time delay but different Doppler characteristics.

Points distributed on coaxial cones, provide the same Doppler shifts of the backscattered waves but different time delays. Targets on a specific hyperbola, which can be seen in Figure 2.13, will provide equi- Doppler returns. Thus if the time delay

and Doppler information in the backscattered waves are processed simultaneously, the surface can be divided into a coordinate system of concentric circles and coaxial hyperbolas, and each point on the surface can be uniquely identified by a specific time delay and specific Doppler. The resolution capability of the imaging system is thus dependent on the measurement accuracy of the differential time delay and differential Doppler (or phase) between two neighbouring points on the surface.

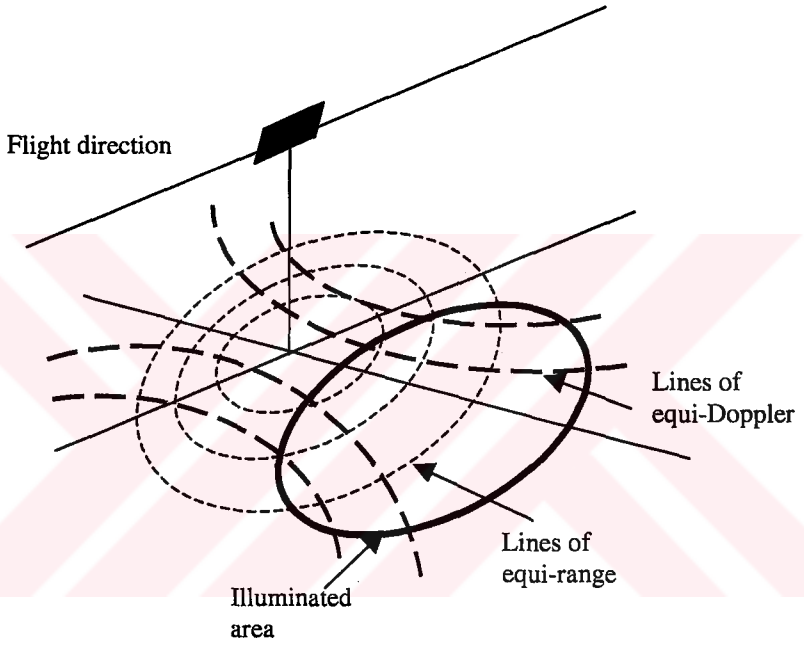

Figure 2.13. Coordinate system for SAR image formation

The radar sends a pulse to obtain the time delay information. To obtain the Doppler information properly, backscattered waves from many successive pulses are needed with an acceptable pulse repetition frequency (PRF). Hence, as the illuminated areas pass over a certain region, the received signals have a Doppler information and range information for each point on the surface which is illuminated. These information are then processed to identify uniquely each point on the region and generate the image. A large number of operations are needed to generate each pixel in the image.

There are some restrictions on the limits of PRF; it cannot be chosen freely. If the PRF is determined so high, returned signals from two successive transmitted pulses arrive at the same time, this will cause range ambiguity. Similarly, if the PRF is

chosen very low, returned signals will not be sampled properly; it will cause azimuth ambiguity.

The upper limit of the PRF is produced according to the following approach:

A view of the SAR system in range direction is given in Figure 2.14.

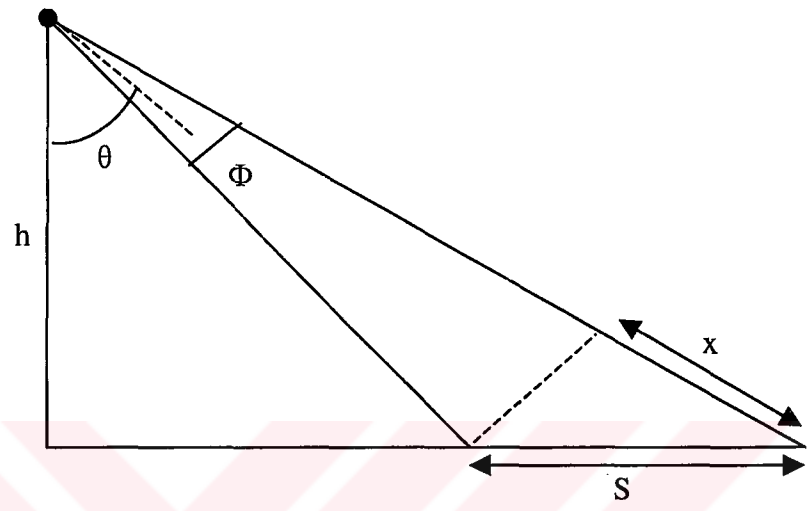

Figure 2.14.SAR viewing geometry in the range plane

In order to avoid the situation in which the far edge echo arrives at the sensor simultaneously with the near edge echo, it is necessary that;

$$T > \frac{2.x}{c} \tag{2.14}$$

$$T > \frac{2.h}{c}.\frac{\tan\theta}{\cos\theta}.\Phi = \frac{2.\lambda.h}{c.W}.\frac{\sin\theta}{\cos^2\theta} \tag{2.15}$$

or

$$PRF < \frac{c.W}{2.\lambda.h}.\frac{\cos^2\theta}{\sin\theta} \tag{2.16}$$

where T is the time between successive pulses, θ is the look angle, W is the antenna width, Φ is the beamwidh (that is $\Phi=\lambda/W$) in range direction, h is the platform height, S is the swath width, x is the difference between far and near ranges of the swath. In this analysis, Φ is assumed to be small.

The lower limit of the PRF is determined by the necessity that PRF must exceed the maximum Doppler shift of the backscattered signals. Note that targets in boresight will return signals with zero Doppler shift. If a backscattered signal of a target is shifted in frequency by an amount equal to the PRF, the sensor cannot distinguish this signal from that of a target in boresight. Hence, PRF has to be high enough to exceed the maximum Doppler shift of targets located at beam edge.

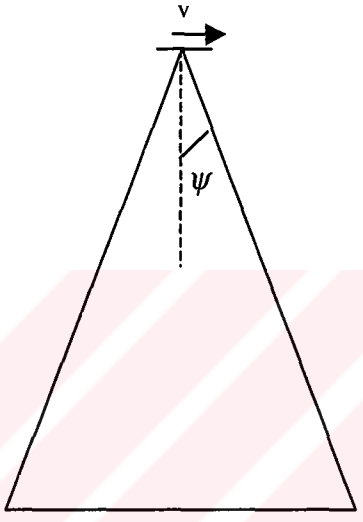

Figure 2.15. SAR viewing geometry in the azimuth plane

Referring to Figure 2.15, $v_r = v.\sin\psi \approx v.\psi$, where ψ is the beamwidth in azimuth direction (that is ψ=λ/L), by using Equation 2.12;

$$PRF_{low} = f(x_R) = \frac{2.v}{L} \tag{2.17}$$

The two limitations derived above give

$$\frac{c.W}{2.\lambda.h}.\frac{\cos^2\theta}{\sin\theta} > PRF > \frac{2.v}{L} \tag{2.18}$$

This condition implies a minimum size of the antenna area ($W.L$) such as;

$$W.L > \frac{4.v.\lambda.h.\sin\theta}{c.\cos^2\theta} \tag{2.19}$$

2.3. Focusing Procedure

Focusing usually corresponds to data processing. Azimuth resolution becomes independent from range distance via focusing. In unfocused SAR, locating the target is limited to a time interval over which the Doppler frequency is approximately constant. This causes errors in processing, but a better performance is achieved compared with real aperture radars. For unfocused SAR, azimuth resolution is evaluated as [7];

$$\Delta x = \sqrt{\frac{\lambda.R}{2}} \tag{2.20}$$

In focused SAR, the full phase variation over the entire time – interval in which the target is in the antenna beam is taken into account in the processing. As explained before, azimuth resolution is independent of range for focused SAR case.

Here, it is useful to investigate phase history of a target for a spaceborne SAR and range migration effect which is an important parameter in spaceborne SAR systems. A precise estimation of the phase histories play an important role in accuracy of the matched filter which is used for azimuth processing and in turn azimuth resolution. Let us consider the imaging geometry for a spaceborne SAR given in Figure 2.16. $\mathbf{R}_T$ refers to the position vector of a target on the Earth' s surface. $\mathbf{R}_{SC}$ refers to the position vector for the spacecraft.

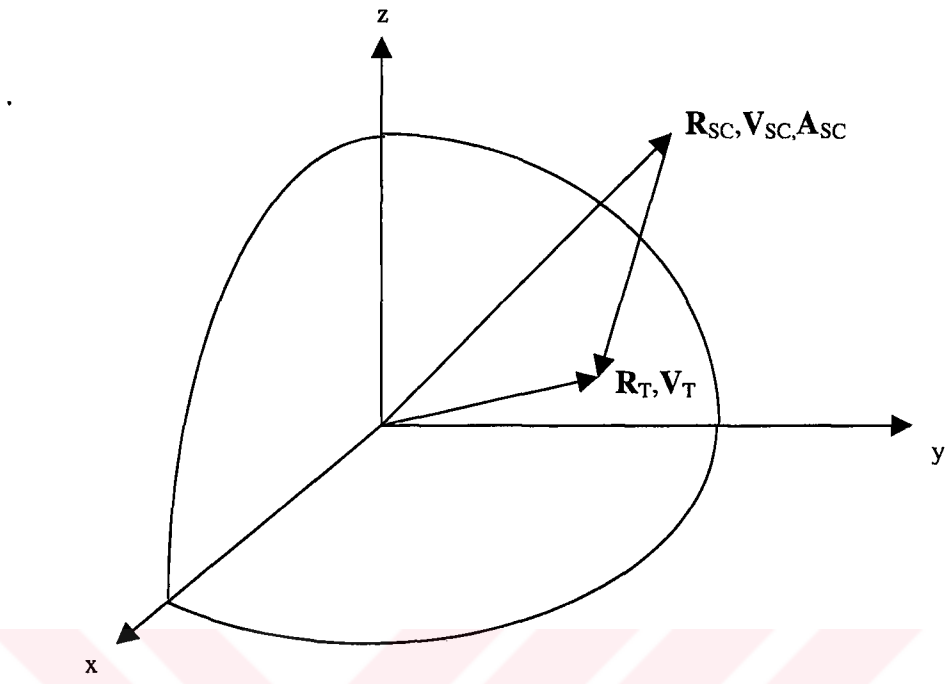

Figure 2.16. Imaging geometry of a spaceborne SAR

The phase history of the target located at $\mathbf{R}_T$ is given by;

$$\phi(t) = \frac{4\pi}{\lambda} |\mathbf{R}_T(t) - \mathbf{R}_{SC}(t)| \tag{2.21}$$

The instantaneous Doppler frequency is;

$$f(t) = -\frac{2}{\lambda} \cdot \frac{d}{dt} |\mathbf{R}_T(t) - \mathbf{R}_{SC}(t)| \tag{2.22}$$

Modeling the target' s motion as a point on the surface of a rotating Earth, $\mathbf{R}_T(t)$ is approximately;

$$\mathbf{R}_T(t) \approx \mathbf{R}_T(0) + \mathbf{V}_T(0).t \tag{2.23}$$

where $\mathbf{V}_T(0) = \mathbf{w}_e \times \mathbf{R}_T(0)$ and $\mathbf{w}_e$ is the Earth' s angular velocity. For small t, spacecraft' s motion is modeled as;

$$\mathbf{R}_{SC}(t) \approx \mathbf{R}_{SC}(0)+\mathbf{V}_{SC}(0).t+(1/2).\mathbf{A}_{SC}(0).t^2 \quad (2.24)$$

where $\mathbf{V}_{SC}(0)$ and $\mathbf{A}_{SC}(0)$ are the velocity and acceleration vectors of the spacecraft at t=0 (i.e when the target is in minimum range). Retaining terms to t^2;

$$f(t) \approx -\frac{2}{\lambda}.\frac{d}{dt}[\,\mathbf{R}_r.\,\mathbf{R}_r+2(\mathbf{R}_r.\,\mathbf{V}_r).t+(\mathbf{V}_r.\,\mathbf{V}_r-\mathbf{R}_r.\,\mathbf{A}_{SC}).t^2\,]^{1/2} \quad (2.25)$$

where

$$\mathbf{R}_r = \mathbf{R}_T(0)-\mathbf{R}_{SC}(0) \quad (2.26)$$

$$\mathbf{V}_r = \mathbf{V}_T(0)-\mathbf{V}_{SC}(0) \quad (2.27)$$

and

$$\mathbf{A}_{SC} = \mathbf{A}_{SC}(0) \quad (2.28)$$

Equation for instantaneous Doppler frequency can be approximated by two terms;

$$f(t) \approx f_{DC} + f_{DR}(t) \quad (2.29)$$

where

$$f_{DC} = -\frac{2}{\lambda.R_{rel}}.\,\mathbf{V}_r.\mathbf{R}_r \quad (2.30)$$

$$f_{DC} = -\frac{2}{\lambda.R_{rel}}(\,\mathbf{V}_r.\,\mathbf{V}_r-\mathbf{R}_r.\,\mathbf{A}_{SC}) \quad (2.31)$$

with

$$R_{rel} = |\,\mathbf{R}_T(t)-\mathbf{R}_{SC}(t)\,| \quad (2.32)$$

These two terms f_{DC} and f_{DR} are called Doppler centroid and Doppler frequency rate, respectively. Accurate estimation of these two terms is important since obtained images via filtering are affected in view of resolution. Note that in our study Earth rotation is neglected. Thus, $\mathbf{w}_e = 0$; this condition results in stationarity of target and a constant target range.

Another concept which must be considered is the range migration effect. Range migration is the general name for range curvature and range walk effects. These are undesired phenomenons caused by range variation as the radar sensor is in motion. Range walk and range curvature can be neglected for airborne SAR systems since range variation is not great. However, in spaceborne SARs they are not negligible as the amount of the range to the target and variation of range at every instant of time are much greater. Illustrations for range curvature and range walk are given in Figure 2.17 and Figure 2.18.

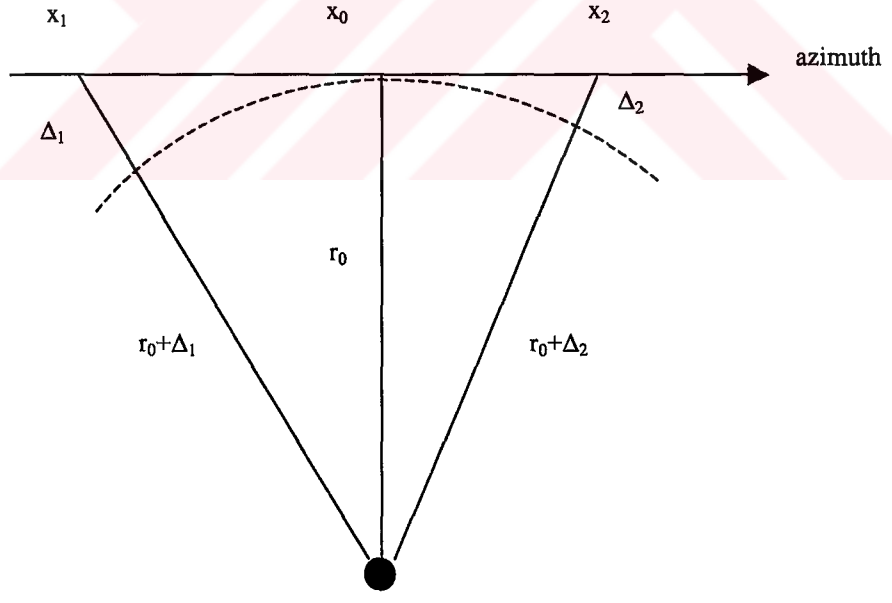

Figure 2.17. Distance history of a point target

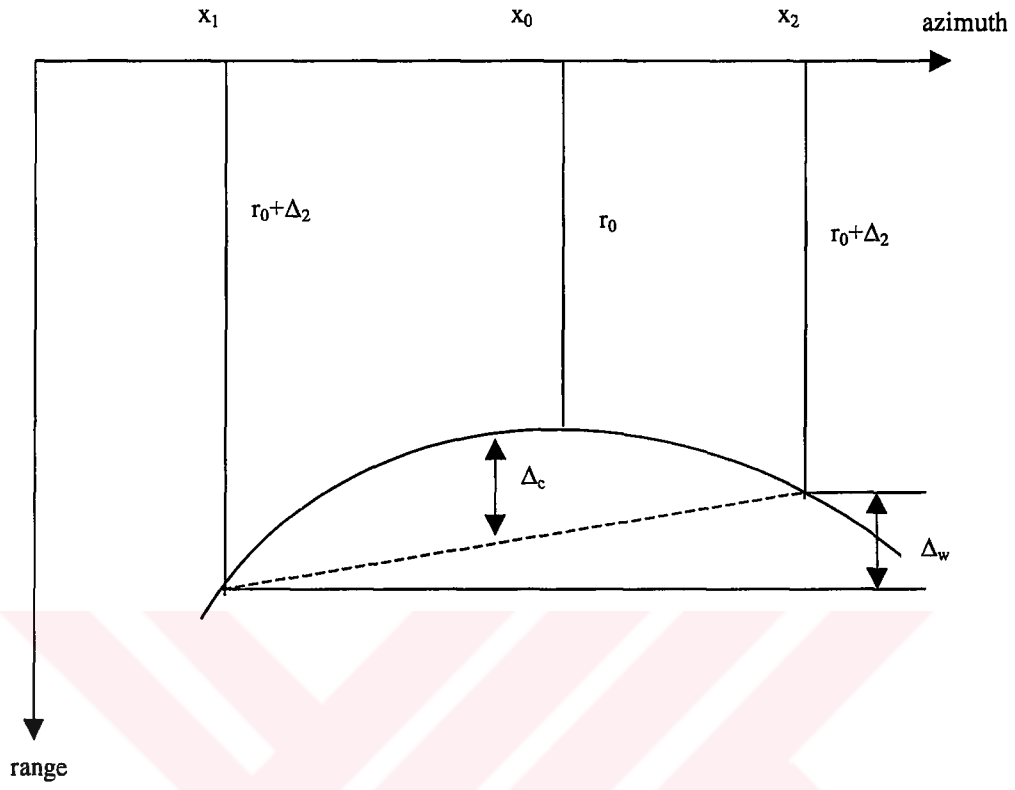

Figure 2.18. Range migration effect

The locus of a point target represent a section of a curve. This phenomenon is called range curvature (Δ_c). Range walk (Δ_w) is the difference between different measured ranges for a point target. Range migration effect is usually compansated in processing algoritms. For instance, in range – Doppler algorithm, a separate step is applied to compansate range walk and range curvature effects.

2.4. ERS – 2 Raw Data Processing

2.4.1. ERS – 2 Raw Data Set

In this study ERS – 2 raw data, which cover a 100 km x 100 km area which is shown in Figure 2.20 (with the permission of ESA – European Space Agency) are processed via different algorithms. Raw data set has 5616 x 28000 complex samples in range and azimuth directions respectively as given in Figure 2.19. In azimuth direction, 28000 pulses are produced to illuminate the region to be imaged. Successive coherent radar returns are received; each backscattered signal is sampled by a suitable sampling frequency and 5616 discrete values are obtained. Obtained data are quantized with 5 bits.

Time difference between any two consecutive azimuth samples is 1/PRF (Pulse Repetition Frequency) and distance between in any two successive azimuth samples is v / PRF. Hence, a uniform sampling is applied in both time and spatial domains for azimuth direction. In range direction, a uniform sampling is performed in time domain while a nonuniform sampling is considered in spatial domain since mapping between time and spatial domains is not linear. For example, ground distance between two successive spatial samples nearest to the sensor for a particular beam is 17 m while the last two samples are separated with 23 m.

The procedure that is followed in our processing scheme is to choose a certain amount of data samples in raw data array and operate on this chosen part. Hence, we process on geographical regions whose dimensions are smaller than 100 km x 100 km. For example, a data set of 1024x1024 samples refer to a region approximately 92.966 km^2 (4.544 km in azimuth, 20.460 km in range) and 2048x2048 samples correspond to an area of 372.230 km^2 (9.092 km in azimuth, 40.940 km in range). However, there is a limitation on the choice of data set dimensions. This is because a certain number of samples are needed to fully focus a point target. Synthetic aperture length for a point target is $\lambda.R / L$ as mentioned before. Consider a target at a range of 850000 m (around midswath). A number of 1083 samples can be taken within the full syntetic aperture. Hence, we need 1083 samples to fully focus this point target; choosing 1024 samples in azimuth direction will not be enough because none

of the points will be fully focused. Remembering we use Fast Fourier Transform (FFT) we need at least 2048 samples. Moreover, as the range increases, the number of samples to focus a point target will increase as well. For a data set of certain dimensions, the number of fully focused targets will decrease as a function of range.

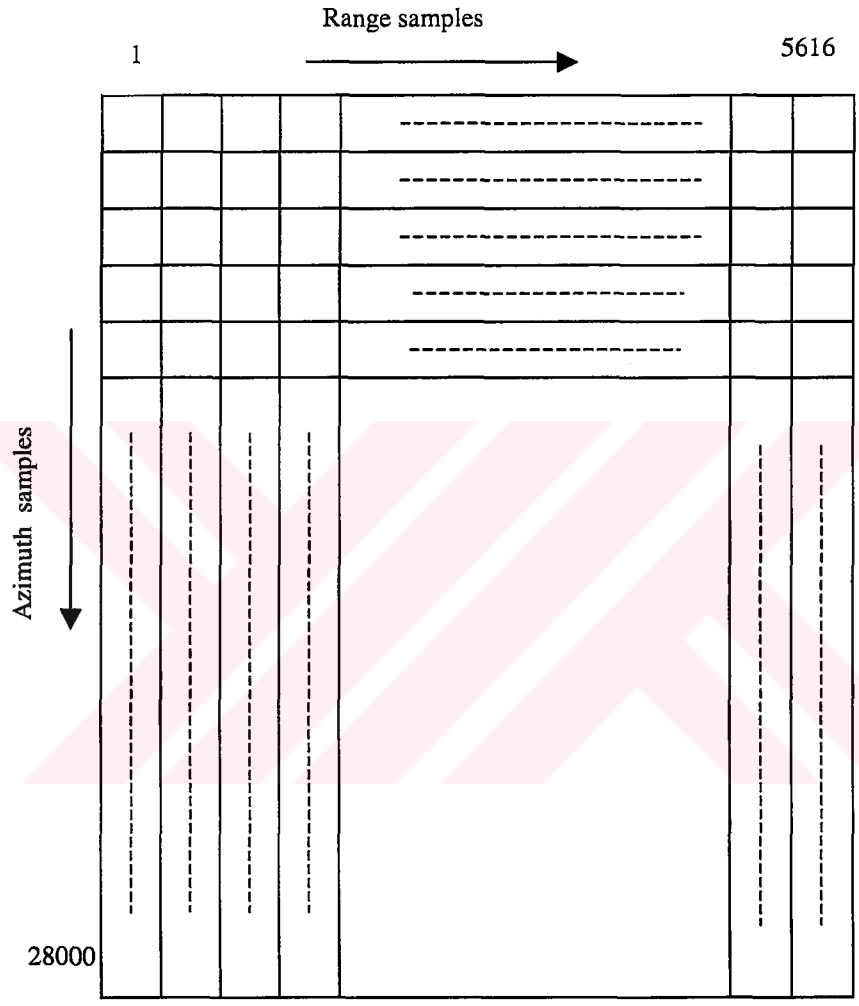

Figure 2.19. Schematic diagram of raw data array

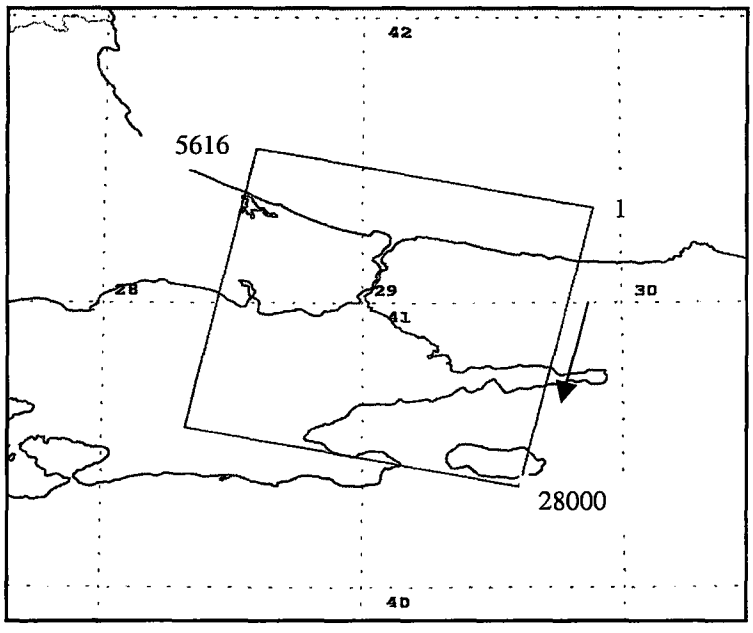

Figure 2.20. Processed region

2.4.2. SAR Transfer Function

Consider the system geometry given in Figure 2.21, where the usual cylindrical coordinate system (x, r, θ) is used with its x – axis coincident with the azimuth direction which is assumed to be a straight line. Here, R is the sensor – target distance (range), r is the shortest sensor – target distance and θ is the angle between r and platform trajectory. x_n is the nth position of the real antenna for an 2N+1 equally spaced positions while n = -N,...,N.

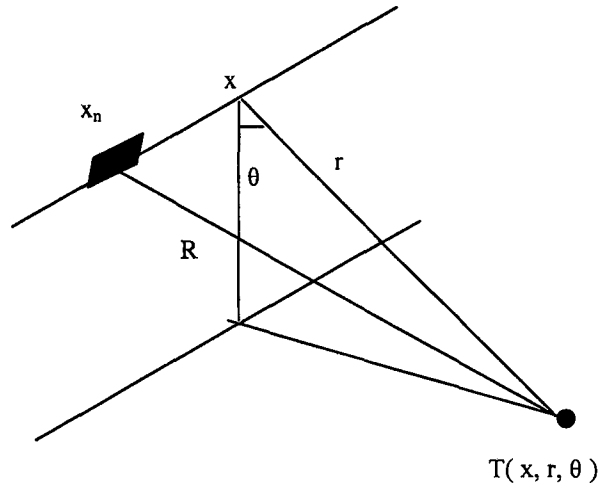

Figure 2.21. Cylindirical coordinate system geometry

In a SAR system, recorded raw signal $h(.)$ can be obtained in terms of impulse response of the system $g(.)$, which is defined as the signal backscattered from a point target, and surface reflectivity pattern $\gamma(.)$.

$$h(x',r') = \iint \gamma(x,r)\, g(x'-x, r'-r, r)\, dx\, dr \tag{2.33}$$

In this proposed system, unprimed coordinates corresponds to ground variables, which are used to locate targets on the ground. Primed variables are called azimuthal variables which are functions of azimuthal time. That is,

$$x' = v t_n \tag{2.34}$$

$$r' = \frac{c t'}{2} \tag{2.35}$$

where

$$t' = t - t_n - 2r/c \tag{2.36}$$

Equation 2.33 shows that the SAR imaging problem can be managed via an appropriate filter operation that recovers an estimation of the reflectivity pattern $\hat{\gamma}(.)$

starting from the received signal. Thus, we must obtain $g(.)$ to find $\hat{\gamma}(.)$, as we already have the raw signal $h(.)$. If the dependence of $g(.)$ on r is neglected, Equation 2.33 can be written as a two – dimensional (2D) convolution:

$$h(x',r') = \iint dx.dr.\gamma(x,r).g(x'-x,r'-r) = \gamma(x',r') \otimes g(x',r') \tag{2.37}$$

In frequency domain;

$$H(\xi,\eta) = \Gamma(\xi,\eta).G(\xi,\eta) \tag{2.38}$$

where $H(\xi,\eta)$, $\Gamma(\xi,\eta)$ and $G(\xi,\eta)$ are the 2D Fourier transforms (FT) of $h(x',r')$, $\gamma(x',r')$ and $g(x',r')$ respectively. $G(\xi,\eta)$ is called transfer function of the system. The simplification considered in Equation 2.37 is often not allowed and r dependence of $g(.)$ requires a special care during SAR data processing.

When r dependence of $g(.)$ is taken into account, the expression for the transfer function $G(\xi,\eta,r)$ is obtained as [1];

$$G(\xi,\eta,r) = \frac{\pi}{\sqrt{a.b.(r_0/r)}}.rect\left[\frac{\eta}{2.b}\right].w^2\left[-\frac{\xi}{2.a}\right].\exp[-j.\Psi(\xi,\eta,r)] \tag{2.39}$$

$$G(\xi,\eta,r) \approx \left(\frac{\pi}{\sqrt{a.b}}\right).rect\left[\frac{\eta}{2.b}\right].w^2\left[-\frac{\xi}{2.a}\right].\exp[-j.\Psi(\xi,\eta,r)] \tag{2.40}$$

where r_0 is the closest range between the platform and the center of the footprint, as explained in Figure 2.22 and Figure 2.23, $w[.]$ is the ground illumination function and $\Psi(\xi,\eta,r)$ is the phase term.

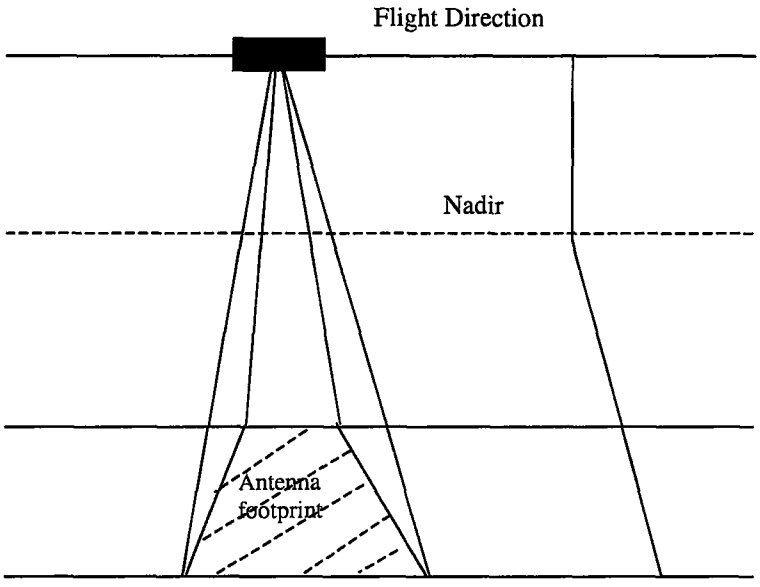

Figure 2.22. Illumination geometry

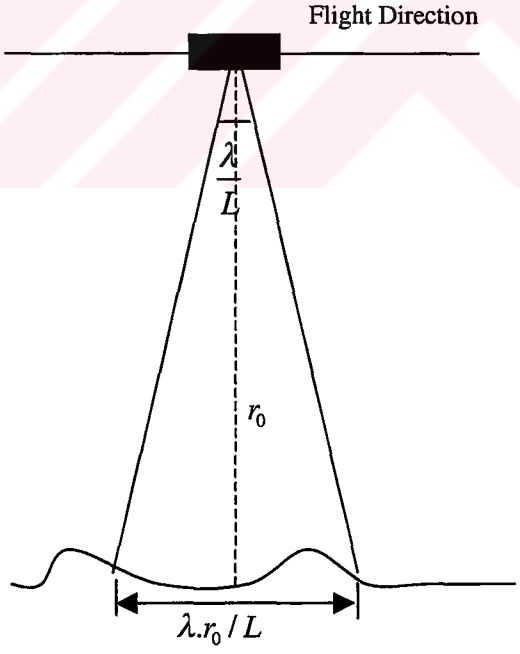

Figure 2.23. Illustration for range distance r_0

Constants a and b are equal to;

$$a = \frac{2\pi.\lambda.r_0}{L^2} \tag{2.41}$$

$$b = \pi.\Delta f.\tau \tag{2.42}$$

Here, λ is wavelength, L is antenna dimension in azimuth direction. For simplicity, a uniform illumination over the ground is assumed;

$$w^2\left[-\frac{\xi}{2.a}\right] \approx rect\left[\frac{\xi}{2.a}\right] \tag{2.43}$$

can be made. Phase term $\Psi(\xi,\eta,r)$ is evaluated as [1];

$$\Psi(\xi,\eta,r) = \frac{\eta^2}{4.b} - 2.a.\left(\frac{L}{\lambda}\right)^2.\left(1+\varepsilon.\frac{\eta}{2.b}\right).\frac{r}{r_0} + \frac{L}{\lambda}.\frac{r}{r_0}.\sqrt{\left(2.a.\frac{L}{\lambda}\right)^2.\left(1+\varepsilon.\frac{\eta}{2.b}\right)^2 - \xi^2} \tag{2.44}$$

$$\varepsilon = \frac{\Delta f}{f} \tag{2.45}$$

Transfer function $G(\xi,\eta)$ is a band limited function between

$$\begin{aligned} -a \le \xi \le a \\ -b \le \eta \le b \end{aligned} \tag{2.46}$$

This condition can be seen in Figure 2.24. For the square root factor in Equation 2.44, a series expansion around $\xi = 0$ is allowed, because the second term in the square root is much smaller than the first one, this sets the phase term almost independent of ξ variable. Thus;

$$\sqrt{\left(2.a.\frac{L}{\lambda}\right)^2.\left(1+\varepsilon.\frac{\eta}{2.b}\right)^2-\xi^2}\approx 2.a.\frac{L}{\lambda}.\left(1+\varepsilon.\frac{\eta}{2.b}\right)-\frac{\xi^2.\lambda..L}{4.a.\left(1+\varepsilon.\frac{\eta}{2.b}\right)} \qquad (2.47)$$

We obtain the expression for $\Psi(\xi,\eta,r)$, which is used in our calculations;

$$\Psi(\xi,\eta,r)=\frac{\eta^2}{4.b}-\frac{\xi^2}{4.a.\frac{r_0}{r}\left(1+\varepsilon.\frac{\eta}{2.b}\right)}=\frac{\eta^2}{4.b}-\frac{\xi^2}{4.a.\frac{r_0}{r}.\left(1+\varepsilon.\frac{\eta}{2.b}\right)} \qquad (2.48)$$

Transfer function that is obtained in this section will have a vital role in data processing algorithms, namely narrow focusing and wide focusing, which are examined in the following sections.

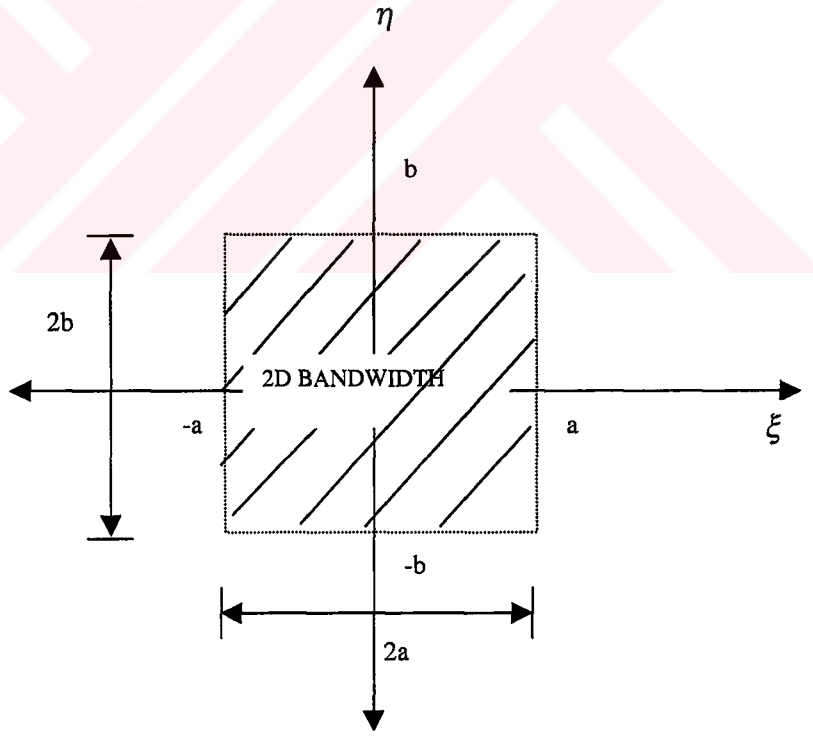

Figure 2.24. 2D signal spectrum for transfer function

2.4.3. Narrow Focusing

Let us extend the point target analysis to the case of an extended illuminated area and terminate the dependence of impulse response (and transfer function) on range by having $r = r_0$. Here, r_0 is the range distance to the center of the chosen area to be imaged. This definition is different from the definition which is explained in point target analysis. In narrow focusing, r – dependence of transfer function is neglected. We have

$$h(x',r') = \iint \gamma(x,r)\, g(x'-x, r'-r, r_0)\, dx.dr \tag{2.49}$$

This expression corresponds to a 2D convolution and SAR data processiong a 2D deconvolution as given in the previous parts. It is convenient to carry out the deconvolution operation in the Fourier domain since it provides computational efficiency. We recast Equation 2.49 according to Equation 2.37;

$$H(\xi,\eta) = \Gamma(\xi,\eta)\, G_0(\xi,\eta) \tag{2.50}$$

$$G_0(\xi,\eta) = G(\xi,\eta,r_0) \tag{2.51}$$

$G_0(\xi,\eta)$ is the 2D Fast Fourier Transform (FFT) of $g(x',r',r_0)$. We can write $\Gamma(\xi,\eta)$ approximately as;

$$\Gamma(\xi,\eta) = H(\xi,\eta)\, G_0^*(\xi,\eta) \tag{2.52}$$

The block diagram of the 2D processing algorithm based on Equation 2.52 is given in Figure 2.25. The key point of the procedure is represented by knowledge of the transfer function obtained in the previous section by assuming $r = r_0$. For this reason we refer to this processing procedure as the ' narrow focusing ' since only the central part of the scene $r = r_0$ is perfectly focused.

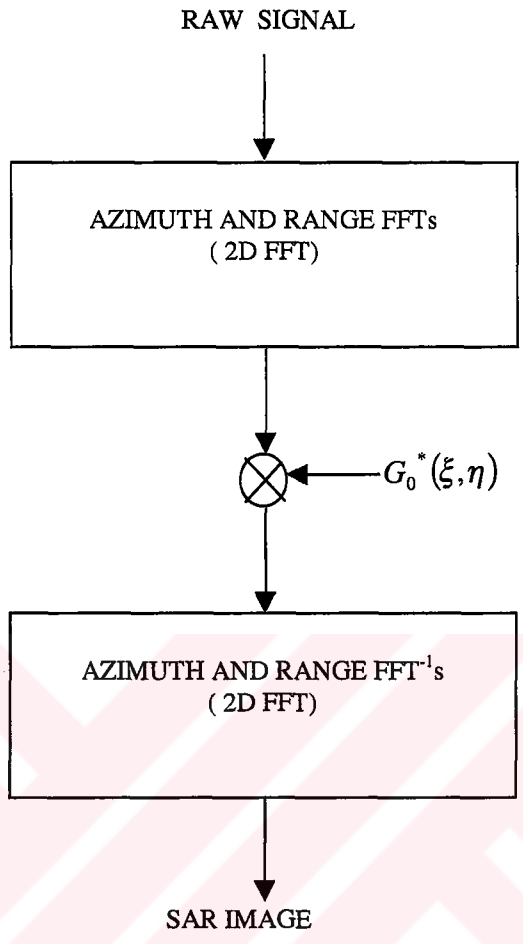

Figure 2.25 Narrow focus SAR processing block diagram

Narrow focus processing result for a region of the Bosphorus, Istanbul can be seen in Figure 2.26. Four sets of raw data, 1024 x 1024 samples per each, are combined to construct the image. As discussed earlier, while a perfect focus is achieved around image center ($r = r_0$) , artifacts increase towards the edges. Note that during process, before taking 2D FFT^{-1}, Hamming window is applied to data to have a better performance on reconstructed image.

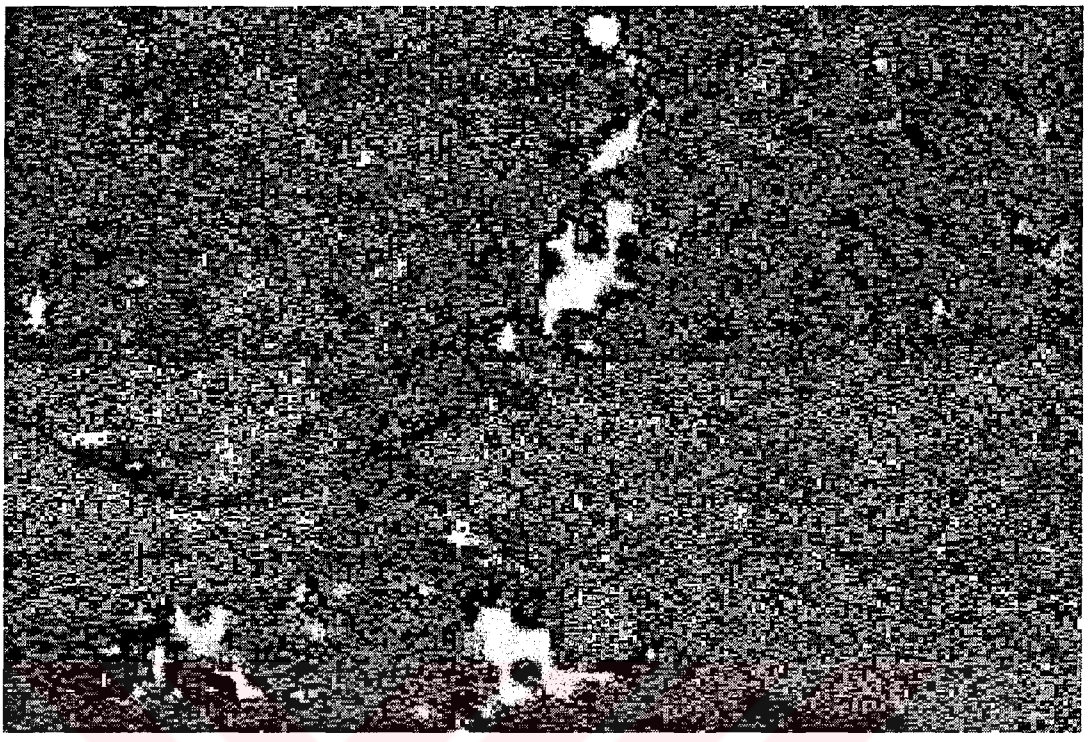

Figure 2.26. Narrow focus result for the Bosphorus, Istanbul (4x1024x1024 samples)

2.4.4. Wide Focusing

Narrow focus processing scheme does not account for range dependence of the transfer function; this is not acceptable in many cases and ways to obtain fully focused image are desirable. This implies moving from a narrow focus to a wide focus processor.

Let us start from decoupling the r – invariant component of the phase term $\Psi(\xi,\eta,r)$ from the r – variant one [1];

$$\Psi(\xi,\eta,r)=\Psi_0(\xi,\eta)+(r-r_0).K(\xi,\eta) \tag{2.53}$$

where

$$K(\xi,\eta)=-\frac{2.a}{r_0}.\left(\frac{L}{\lambda}\right)^2.\left(1+\varepsilon.\frac{\eta}{2.b}\right)+\frac{L}{\lambda.r_0}.\sqrt{\left(2.a.\frac{L}{\lambda}\right)^2.\left(1+\varepsilon.\frac{\eta}{2.b}\right)-\xi^2} \tag{2.54}$$

$K(\xi,\eta)$ can be written as a series expansion such that;

$$K(\xi,\eta) = \mu(\xi) + \eta.v(\xi) \tag{2.55}$$

Here, $\mu(\xi)$ accounts for imperfections caused by phase variation with changing range and $v(\xi)$ is for the range migration effect. For a negligible range migration (i.e. $v(\xi) = 0$), $K(\xi,\eta)$ reduces to $\mu(\xi)$. Hence,

$$K(\xi,\eta) = \mu(\xi) = -\frac{2.a}{r_0}.\left(\frac{L}{\lambda}\right)^2 + \frac{L}{\lambda.r_0}.\sqrt{\left(2.a.\frac{L}{\lambda}\right)^2 - \xi^2} \tag{2.56}$$

Neglecting amplitude terms;

$$G(\xi,\eta,r) = \exp(-j.\Psi(\xi,\eta,r)) \tag{2.57}$$

$$G(\xi,\eta,r) = G_0(\xi,\eta).\exp(-j.(r-r_0).\mu(\xi)) \tag{2.58}$$

Range dependence of the transfer function generates a nonlinear mapping in the range frequencies of the spectrum of $\gamma(.)$ such as;

$$H(\xi,\eta) = \Gamma[\xi,\eta + \mu(\xi)].G_0(\xi,\eta) \tag{2.59}$$

Equation 2.59 suggests the following processing strategy whose block diagram is depicted in Figure 2.27 :

As the first step we compute the 2D spectrum of the SAR raw data $H(\xi,\eta)$, then multiply it by $G_0^*(\xi,\eta)$ according to following approximation:

$$\Gamma[\xi,\eta + \mu(\xi)] \approx H(\xi,\eta).G_0^*(\xi,\eta) \tag{2.60}$$

The second processing step consists of a range FFT^{-1} (1D FFT^{-1}). η - FFT^{-1} can be expressed as;

$$FFT^{-1}\left[H(\xi,\eta)G_0^*(\xi,\eta)\right] \approx \exp(-j.\mu(\xi).r').\hat{\gamma}(\xi,r') \qquad (2.61)$$

Variation of $\mu(\xi)$ as a function of number of samples in azimuth direction (n) for r_0 = 846417 m, a = 3010, L = 10 m and λ = 0.0566 m (wavelength for carrier frequency) for 1024x1024 data region is given in Figure 2.28. It can be seen that $\mu(\xi)$ varies symmetrically; it means a symmetrical phase correction, which is minimum in the image center and increasing towards edges in azimuth direction, is applied on the image.

We aim to obtain $\hat{\gamma}(\xi,r')$. Hence, as the third step, we must multiply the resultant expression by $\exp(+j.\mu(\xi).r')$ in $\xi - r'$ domain:

$$\hat{\gamma}(\xi,r') = FFT^{-1}\left[H(\xi,\eta)G_0^*(\xi,\eta)\right]\exp(+j.\mu(\xi).r') \qquad (2.62)$$

The last step includes taking ξ - FFT^{-1} to obtain $\hat{\gamma}(x',r')$, which is the estimation of the reflectivity pattern and desired SAR image. Hamming window is used in ξ domain before ξ - FFT^{-1}. Wide focus processing result for a region of the Bosphorus, Istanbul is obtained as seen in Figure 2.29. A focus which spreads over the whole image and differs from narrow focusing is recognized.

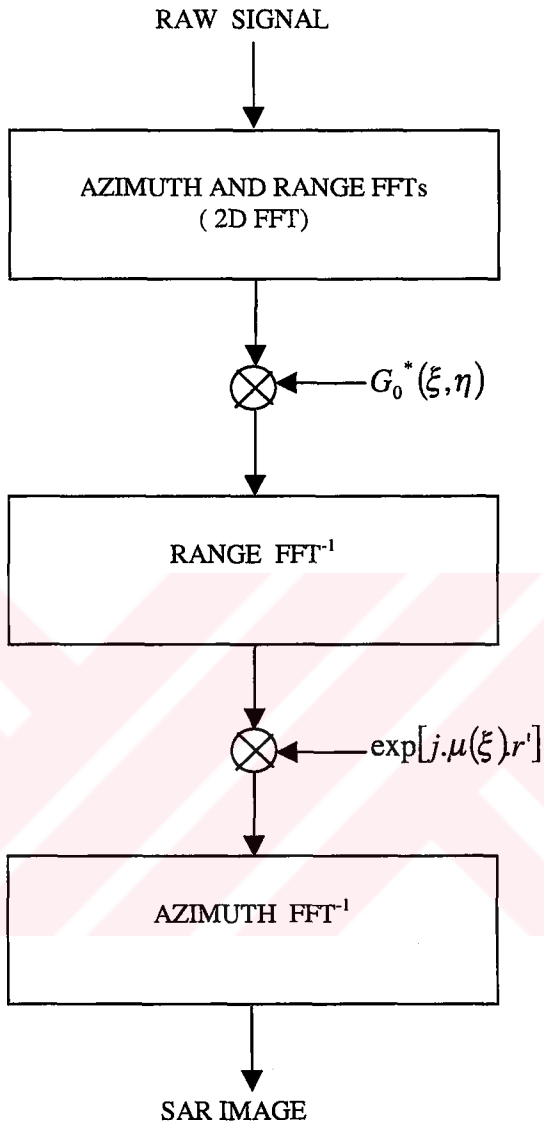

Figure 2.27. Wide focus SAR processing block diagram

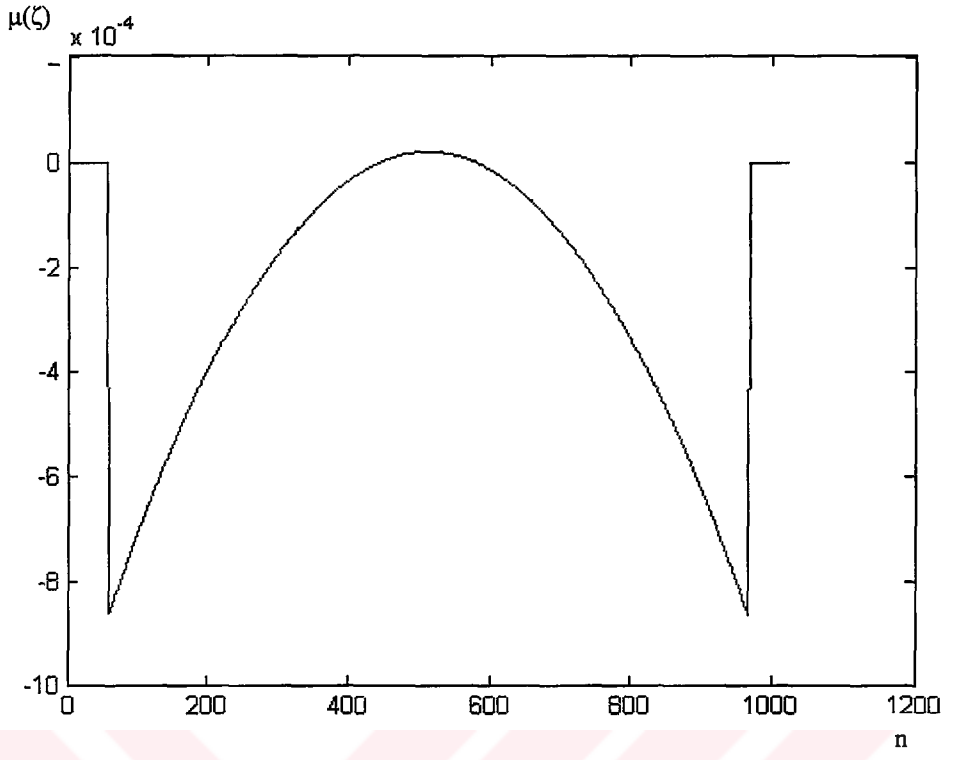

Figure 2.28. μ as a function of n

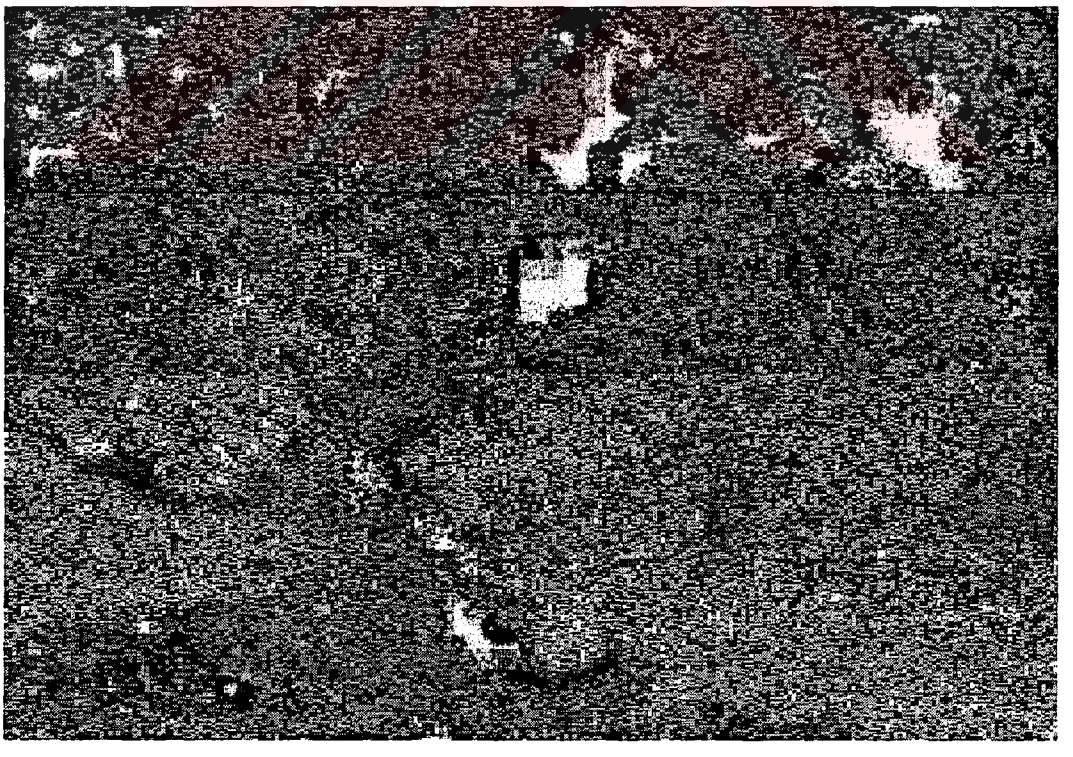

Figure 2.29. Wide focus result for the Bosphorus, Istanbul (4x1024x1024 samples)

3. ANALYSES AND RESULTS

3.1. Introduction

Desired images are reconstructed as explained in the previous section. Images are obtained via plotting the modules of the elements in the processed data matrices. Now, statistical analyses can be carried out on both raw and processed data to understand the nature of the data of interest. Best approach to achieve this goal is to analyze the histograms of the images. Histograms of various sample data are plotted and checked whether they are similar to some known distributions. If so, parameters needed to define these distributions are found.

To improve visual quality of the images, image enhancement methods such as histogram expansion and histogram equalization may be used. We operate histogram expansion on some examples, thus a global enhancement over images are performed.

3.2. Statistical Analysis

Histogram analysis is a remarkable way to analyze images statistically. We construct the histogram by examining the gray level value of each pixel in the image and counting the number of pixels displaying each of the possible values. On the histogram plot, each gray level value is represented by a histogram bin whose height represents the number of image pixels displaying that value. Therefore the process of constructing the histogram corresponds to the filling of histogram bins.

Histogram of an image gives an estimate of the probability of occurrence of gray levels. A plot of this function for all gray levels provides a global description of the appearance of the image. For example, a histogram on which the gray levels are concentrated toward the dark end of the gray scale range means an image with overall dark characteristics. Opposite is true as well. A histogram which has a narrow

shape indicates little dynamic range and thus corresponds to an image having low contrast. As all gray levels occur toward the middle of the gray scale, the image would appear gray.

Although the properties discussed above are global descriptions that say nothing specific about image content, the shape of the histogram of an image does give us useful information about the possibility for contrast enhancement. As we have low contrast images, contrast enhancement would be an important improvement factor.

To obtain histograms, we first normalize data matrix elements between 0 – 255. Thus we have 256 different gray level values. Then, histograms are constructed by the properties discussed above.

Let us consider a 1024x1024 raw data and the image that is produced via narrow focusing given in Figure 3.1

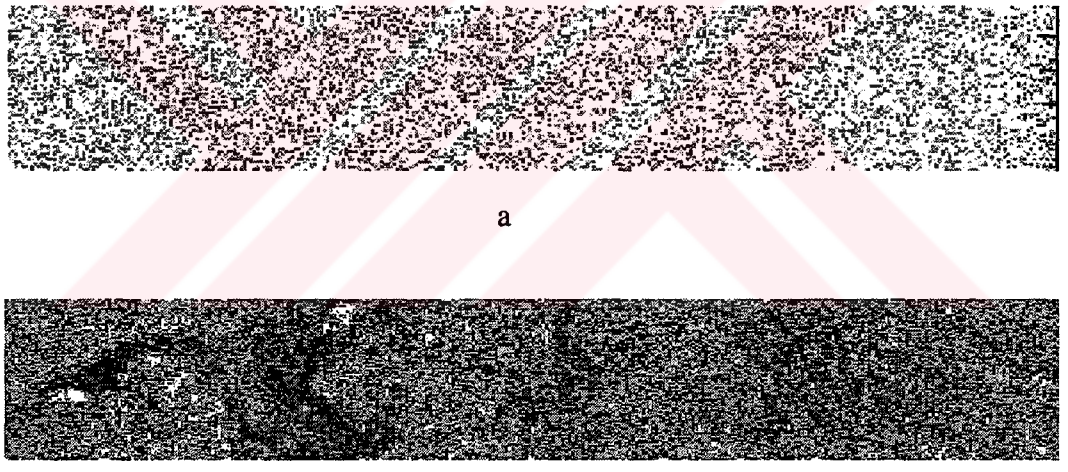

a

b

Figure 3.1. Raw data (a) and image via narrow focusing (b)

Histogram of the processed image can be seen in Figure 3.2. Even if we do not have any information about the image, we can say that it is a dark and a low contrast image since its histogram is mounted around dark gray levels and has a narrow peak. This histogram has a mean of 18.

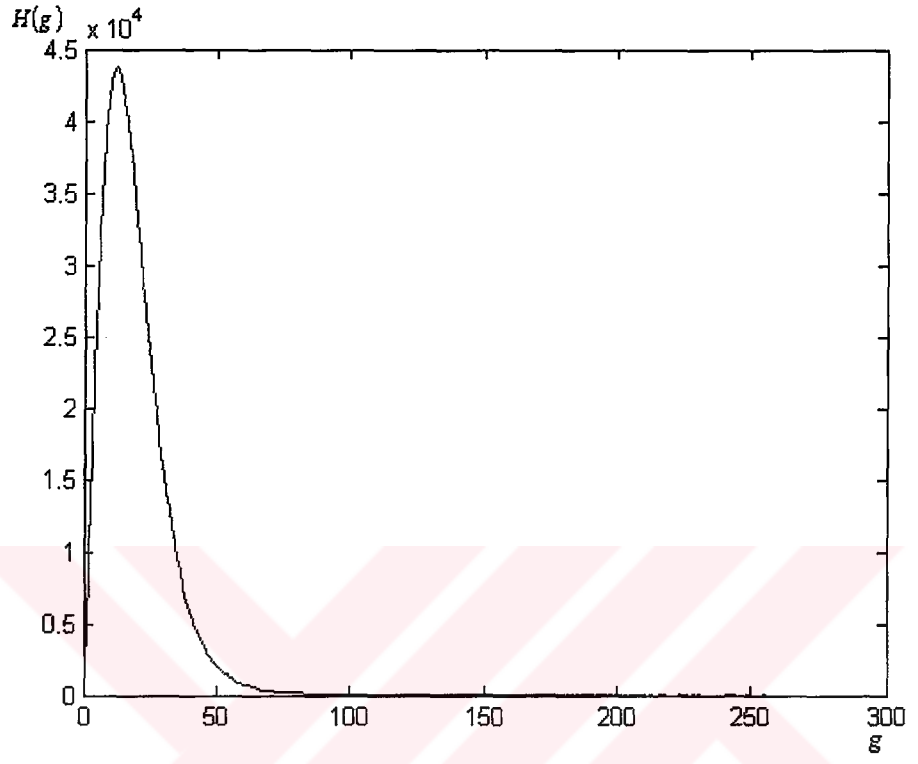

Figure 3.2.. Histogram of the processed image

Distribution observed in Figure 3.2 is quite similar to Rayleigh distribution which is defined as;

$$p(x) = \frac{x}{\sigma^2}.\exp\left(-\frac{x^2}{2.\sigma^2}\right) \quad , \qquad x \geq 0 \qquad (3.1)$$

Rayleigh distribution with the same mean (18)is given in Figure 3.3.

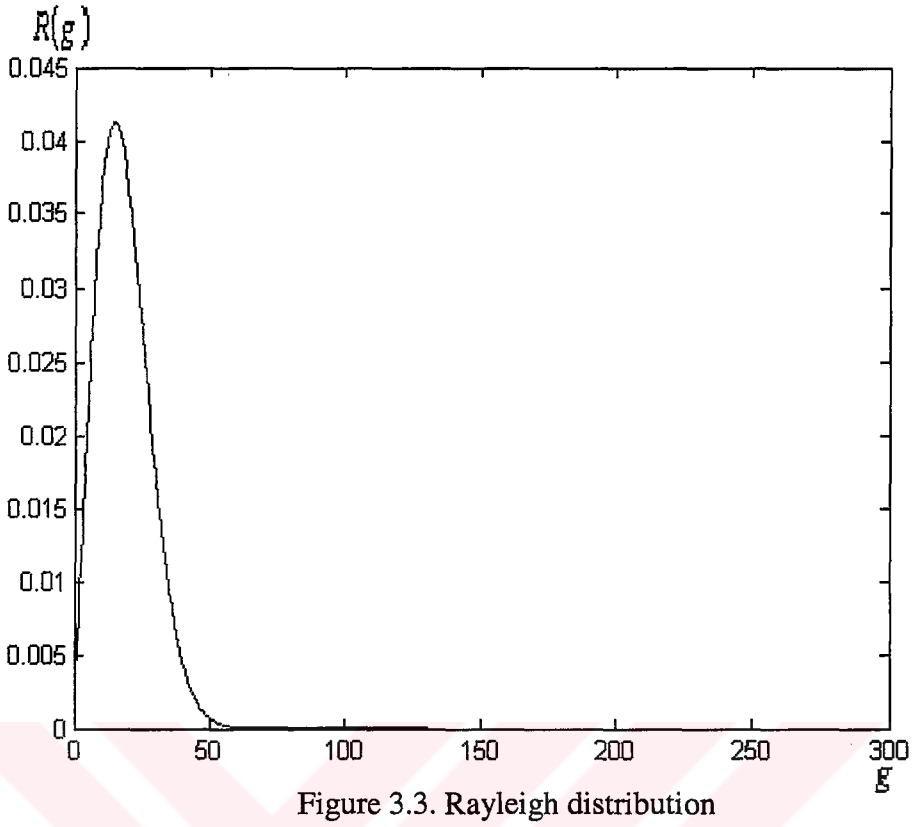

Figure 3.3. Rayleigh distribution

Normalized histogram according to Rayleigh distribution can be seen in Figure 3.4. Histogram of the raw data has also a Rayleigh distribution which is the case in Figure 3.5. Same procedure can be followed for raw data as well.

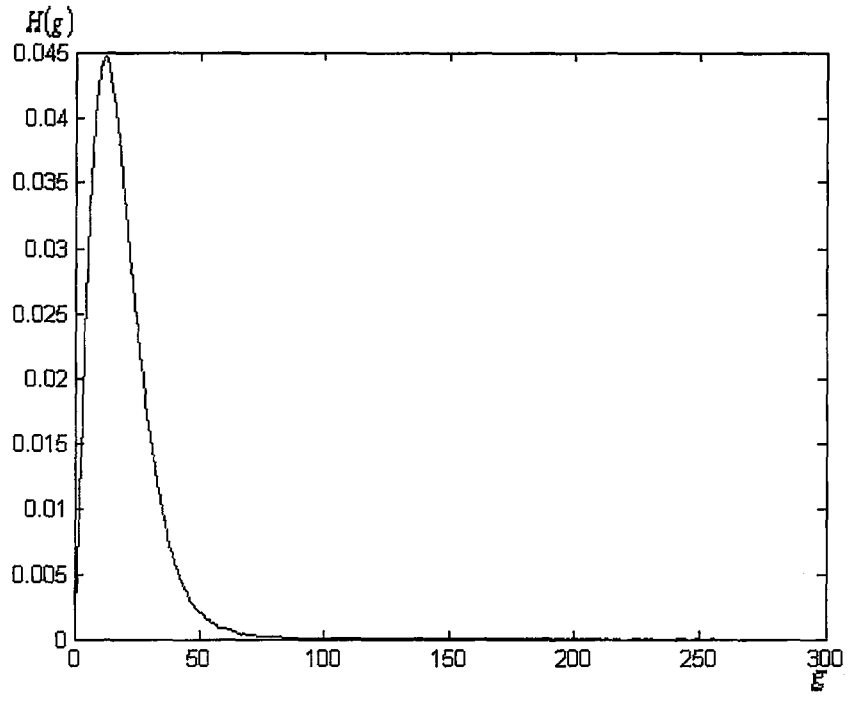

Figure 3.4. Histogram normalized by Rayleigh distribution

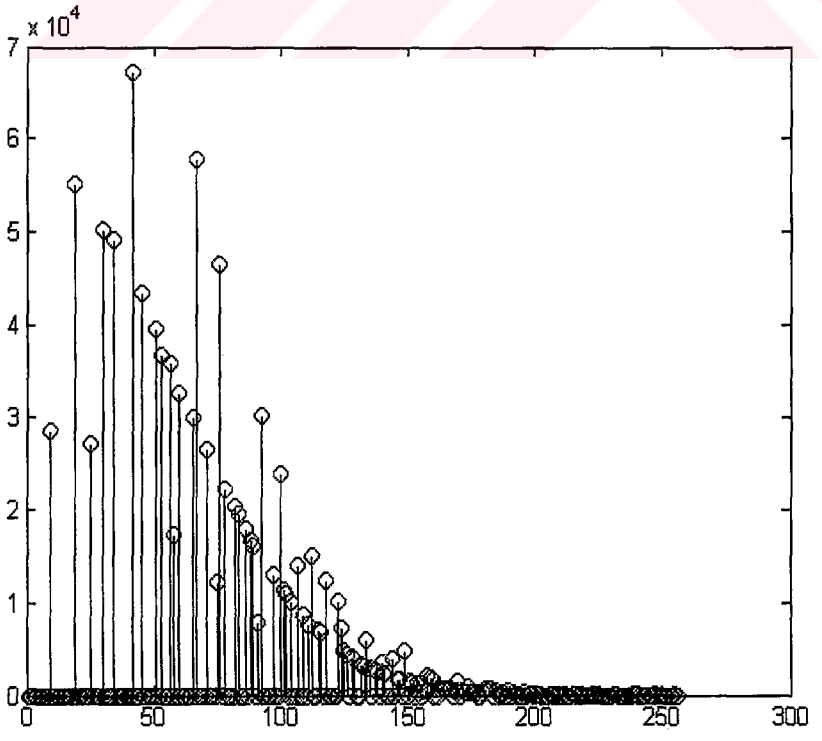

Figure3.5. Histogram of the raw data

An analysis for the whole raw data can also be performed. Variation of total gray levels for range and azimuth is given in Figure 3.6. As we realize, signals backscattered from far range attenuate more compared with the ones from near range. This is natural because attenuation of electromagnetic waves increases with the increasing distance. Moreover, we can see that signals attenuate more in sea rather than ground if we examine the second graph carefully considering the processed region.

Wide focus processing result for a region of the Bosphorus, Istanbul is obtained as seen in Figure 2.29. A focus which spreads over the whole image and differs from narrow focusing is recognized.

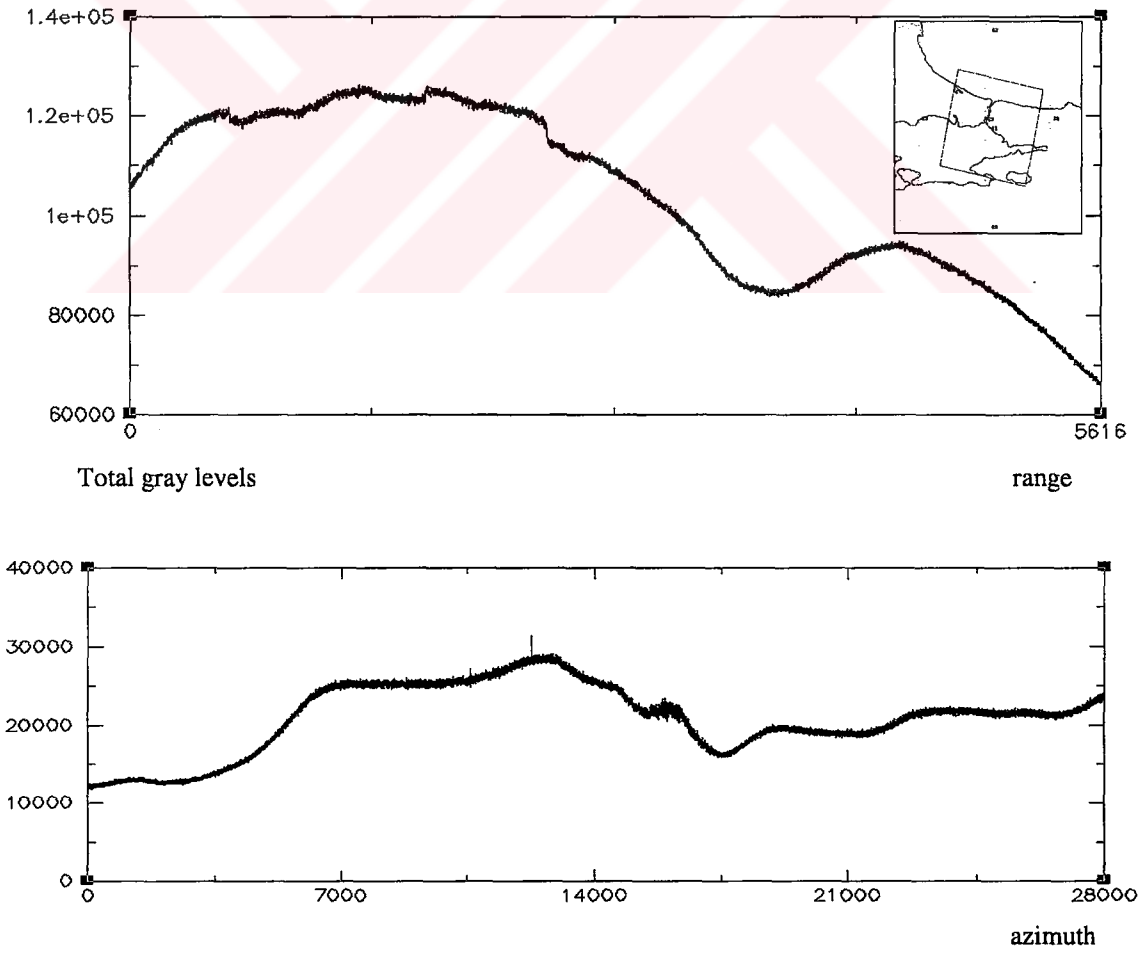

Figure3.6. Total gray level values for range (above) and azimuth (below)

3.3. Image Enhancement

The principle objective of enhancement techniques is to process an image so that the result is more suitable than the original image for a specific application. Image enhancement is treated here as a processing technique to increase the visual contrast of an image in a designated gray level range. Although the degree of enhancement may be subjective, procedures to perform a given type of enhancement can be directly related to the desired purpose. The method described here is a histogram transformation, hence a global enhancement is presented. It generates a new output histogram by modifying the shape of the input histogram according to a specific mapping function that is chosen to enhance contrast in the range of interest. The result of this is that the gray level values of the original image are modified to improve its appearance or effectiveness for visual analysis.

The method applied here is histogram expansion. It is the most straightforward transformation for enhancement. This is a linear transformation that entails an input intensity range to an output intensity range, which typically uses the full dynamic range.

Remember the image in Figure 3.1.b and its histogram. The histogram has a narrow peak, which means the image is a low contrast image. Hence, histogram expansion can be applied on this histogram to use the full dynamic range (that is gray levels are between 0 – 255).

Linear mapping function which is used to expand the example histogram is;

$$y = \frac{x - x_{min}}{x_{max} - x_{min}} \cdot y_{max} \tag{3.2}$$

where x_{min} and x_{max} are the minimum and maximum values of the input histogram, respectively while y_{max} is the upper boundary for the output histogram interval [0, 255]. However, this mapping function is not efficient for narrow-peak and long-tail histograms since their gray level values reach to the minimum and maximum of the full range. Thus, we can define intervals for the input gray levels to eliminate the ones on histogram tails.

Firstly, we choose input histogram interval as [0, 120] by mapping the gray level values which are greater than 120 to 120. As a result, all the values in data matrix are between 0 and 120. Then we apply the expansion formula and obtain the output histogram given in Figure 3.7 where the defined upper bound of the input histogram is denoted by ' parameter '. Contrast improvement of the resulting image is clear.

As a second choice, interval for the input histogram is determined as [0, 80]. Gray levels greater than 80 are mapped to 80 in the data matrix. Application of the formula results in Figure 3.8. Note the peak on the gray level 256, this effect occurs because all the values of 80 in the matrix are mapped to 256. Also, the lower the chosen upper bound, the more significant the effect on the image.

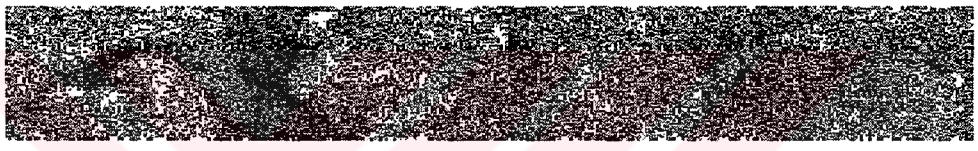

a

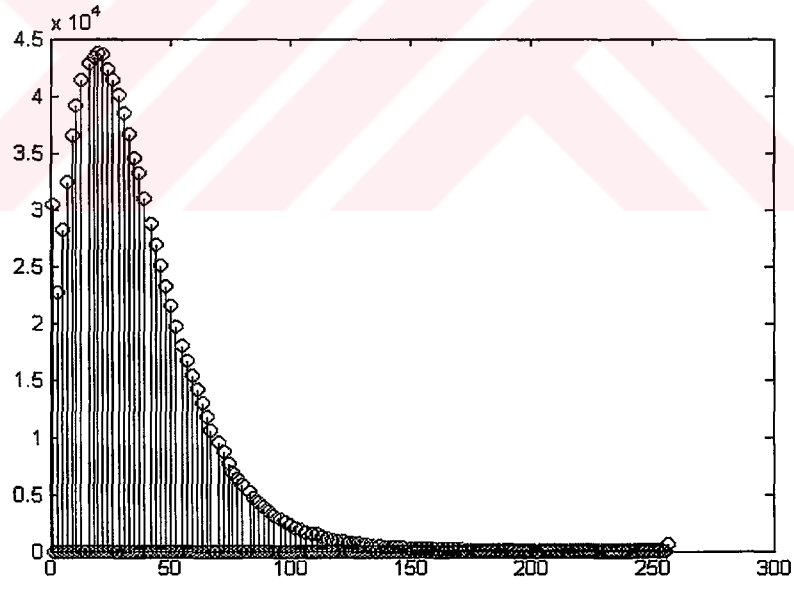

b

Figure 3.7. Improved image and its histogram via histogram expansion (parameter = 120)

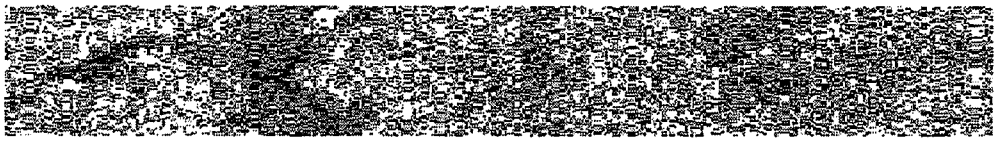

a

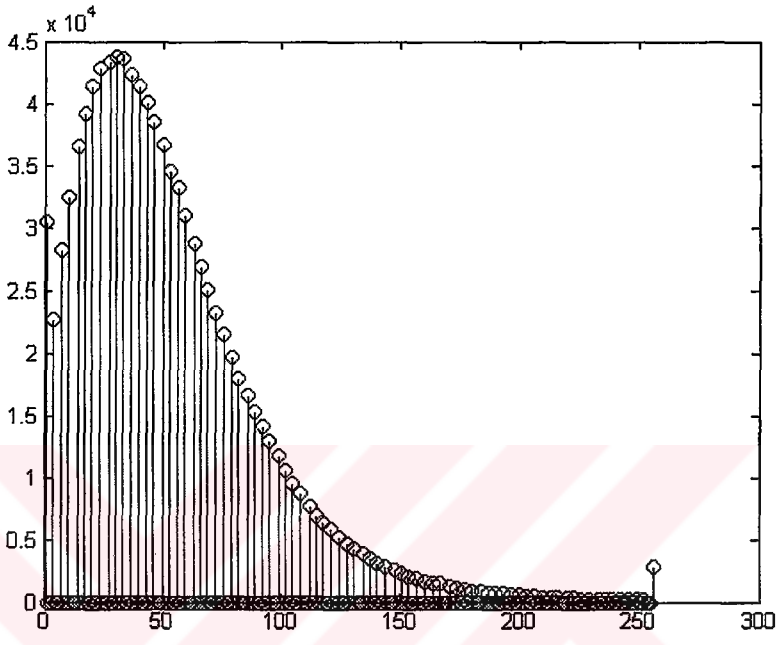

b

Figure 3.8. Improved image and its histogram via histogram expansion (parameter = 80)

Another approach for histogram transformation is the squreroot filter. In this procedure, low gray level values are mapped to higher levels while high gray level values are not modificated as much. Squareroot filter result for a 4x2048x2048 region can be seen in Figure 3.9.

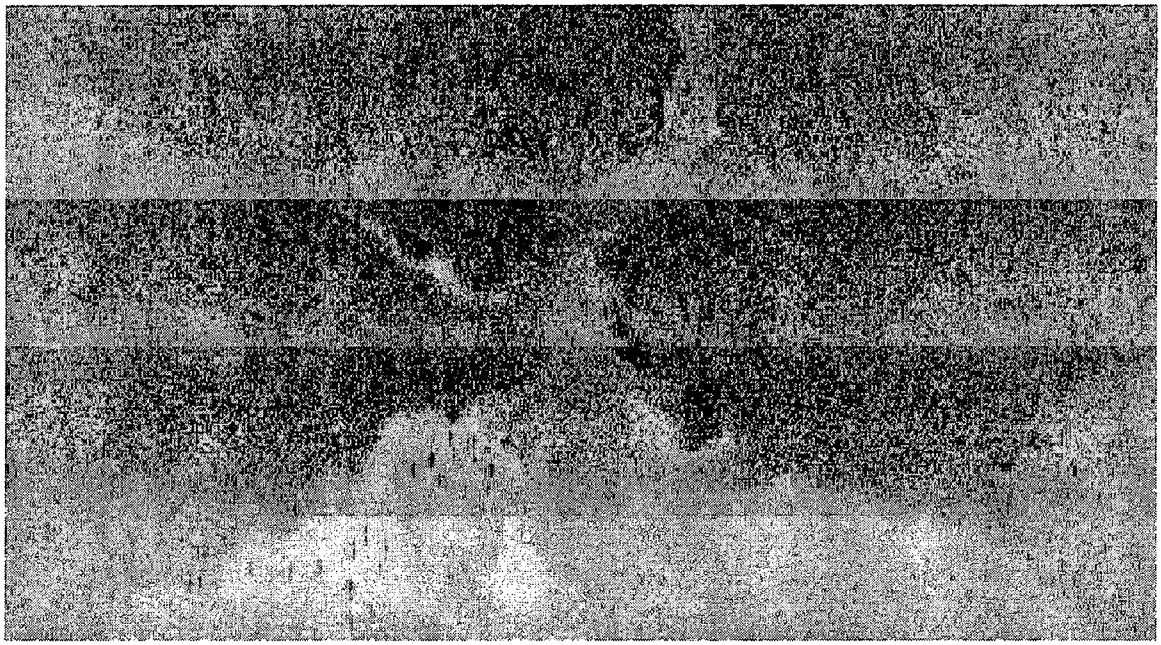

Figure 3.9. Enhanced image via squareroot filter

3.4. Results

We carried out an investigation on SAR theory and SAR raw data processing. We began with utilities of SAR imaging and application areas: It has a wide usage for geological and forest mapping, crop identification, ocean circulation studies, land classification etc. Then we examined previous studies on data processing; presented some bases of focusing algorithms. SAR theory, resolution and other important concepts were presented and Doppler point of view, limits of some parameters such as PRF were clearly explained. In data processing section, facilities of narrow focusing and wide focusing were explained. These algorithms provided efficent results although some aberrations exists in the nature of the processing schemes. Transfer function of the system, which is quite important during process, was analyzed detailly. Operations applied are not for perfect geometries since some approximations are considered. ERS-2 raw data for Istanbul, Turkey were used to compare performances of the algorithms. Images of certain chosen parts of raw data are obtained as we have the chance to process all the raw data. After reconstruction of images, image enhancement methods are applied to improve the visual quality.

Moreover, statistical analysis of both raw and processed data was performed over chosen data. Furher study on raw data is possible via different algorithms; new algorithms which will increase the resolution and handle different aspects of system parameters may be produced.

REFERENCES

[1] **Franceschetti G., Lanari R. and Marzouk E.S.,** 1995. Efficient and High Precision Space – Variant Processing of SAR Data, *IEEE Transactions on Aerospace and Electronic Systems,* **31,** 227 – 237.

[2] **Wu C., Liu K.Y. and Jin M.,** 1982. Modeling and a Correlation Algorithm for Spaceborne SAR Signals, *IEEE Transactions on Aerospace and Electronic Systems,* **18,** 563 – 575.

[3] **Prati C. and Rocca F.,** 1992. Focusing SAR Data with Time – Varying Doppler Centroid, *IEEE Transactions on Geoscience and Remote Sensing,* **30,** 550 – 558.

[4] **Li F.K., Held D.N., Curlander J.C. and Wu C.,** 1984. Doppler Parameter Estimation for Spaceborne Synthetic Aperture Radars, *IEEE Transactions on Geoscience and Remote Sensing,* **23,** 47 – 55.

[5] **Franceschetti, G. and Lanari R.,** 1999. *Synthetic Aperture Radar Processing,* CRC Press, Florida.

[6] **Curlander, J.C. and McDonough, R.N.,** 1991. *Synthetic Aperture Radar: Systems and Signal Processing,* John Wiley&Sons, New York.

[7] **Wehner, D.R.,** 1995. *High Resolution Radar,* Artech House, Boston.

[8] **Goj, W.W.,** 1993. *Synthetic Aperture Radar and Electronic Warfare,* Artech House, Boston.

[9] **Morris, G. and Harkness, L.,** 1996. *Airborne Pulsed Doppler Radar,* Artech House, Boston.

[10] **Mensa D.L.,** 1981. *High Resolution Radar Imaging,* Artech House, California.

[11] **Morchin W.,** 1993. *Radar Engineer' s Sourcebook,* Artech House, Norwood.

[12] **Skolnik M.I.,** 1980. *Introduction to Radar Systems,* McGraw – Hill, Singapore.

[13] **Elachi C., Bicknell T., Jordan R.L. and Wu C.,** 1982. Spaceborne Synthetic – Aperture Imaging Radars: Applications, Techniques and Technology, *Proceedings of the IEEE,* **70,** 1174 – 1209.

[14] **Tomiyasu K.,** 1978. Tutorial Review of Synthetic Aperture Radar with Applications to Imaging of the Ocean Surface, *Proceedings of the IEEE,* **66,** 563 – 572.

[15] **Munson D.C. and Visentin R.L.,** 1989. A Signal Processing View of Strip – Mapping Synthetic Aperture Radar, *IEEE Transactions on Acoustics, Speech and Signal Processing,* **37,** 2131 – 2147.

[16] **Franceschetti G., Migliaccio M., Riccio D. and Schirinzi G.,** 1992. SARAS: A Synthetic Aperture Radar (SAR) Raw Signal Simulator, *IEEE Transactions on Geoscience and Remote Sensing,* **30,** 110- 113.

[17] **Francheschetti G., Lanari R. and Marzouk E.S.,** 1993. Aberration free SAR Raw Data Processing via Transformed Grid Predeformation, *IGARSS' 93,* **4,** 1593 – 1595.

[18] **Berardino P., Marrazzo M., Migliaccio M., Lanari R.,** 2001. ERS-1 / 2 and IFSAR for Antarctica, *IGARSS'01,* **6,** 2554 – 2556.

[19] **Curlander J.C.,** 1984. Utilization of Spaceborne SAR Data for Mapping, *IEEE Transactions on Geoscience and Remote Sensing,* **22,** 106 – 112.

[20] **Freeman A., Johnson W.T.K., Huneycutt B., Jordan R., Hensley S., Siouera P., Curlander J.C.,** The ' Myth ' of the Minimum SAR Antenna Area Constraint, *IEEE Transactions on Geoscience and Remote Sensing,* **38,** 320 – 324.

[21] **Bamler R.,** 1992. A Comparison of Range – Doppler and Wavenumber Domain SAR Focusing Algorithms, *IEEE Transactions on Geoscience and Remote Sensing,* **30,** 706 – 713.

[22] **Bamler R. and Runge H.,** 1991. PRF – Ambiguity Resolving by Wavelength Diversity, *IEEE Transactions on Geoscience and Remote Sensing,* **29,** 997 – 1001.

[23] **Li F.K. and Johnson W.T.K.,** 1983. Ambiguities in Spaceborne Synthetic Aperture Radar Data, *IEEE Transactions on Aerospace and Electronic Systems,* **19,** 389 – 395.

[24] **Madsen S.N.,** 1989. Estimating the Doppler Centroid of SAR Data, *IEEE Transactions on Aerospace and Electronic Systems,* **25,** 134 – 139.

[25] **Moreira A.,** 1993. Suppressing the Azimuth Ambiguities in Synthetic Aperture Radar Images, *IEEE Transactions on Geoscience and Remote Sensing,* **31,** 885 – 888.

[26] **Benz U., Strodl K. and Moriera A.,** 1995. A Comparison of Several Algorithms for SAR Raw Data Compression, *IEEE Transactions on Geoscience and Remote Sensing,* **33,** 1266 – 1268.

[27] **Muff D.G., Blake A.P., Horne A.M.,** 1995. Spaceborne SAR Autofocus, *Recent Developments in Radar and Sonar Imaging Systems: What' s Next?, IEE Colloquium,* **11,** 1110 – 1111.

[28] **Minhui Z.,** 2000. Advance in Synthetic Aperture Radar Activities, *Microwave Conference, 2000 Asia – Pacific,* 474 – 476.

[29] **Heng W.C.A.,** 1997. Synthetic Aperture Radar (SAR) Data Processing, *MSc. Thesis,* National University of Singapore, Singapore.

[30] **Brigham E.O.,** 1990. *The Fast Fourier Transform and Its Applications,* Prentice Hall, New York.

[31] **Gonzalez R.C. and Woods R.E.,** 1993. *Digital Image Processing,* Addison – Wesley, California.

[32] **Seul M., O'Gorman L. and Sammon M.J.,** 2000. *Practical Algorithms for Image Analysis,* Cambridge University Pres, New York.

[33] **Myler H.R.,** 1993. *The Pocket Handbook of Image Processing Algorithms in C,* Prentice Hall, New Jersey.

APPENDIX A

Information on ERS-1 and ERS-2 Satellites

ERS-1

ERS-1 is a European Space Agency (ESA) satellite devoted to remote sensing from a polar orbit. It provides global and repetetive observations of the environment using techniques which allow imaging to take place irrespective of weather conditions.
ERS-1 has a sun – synchronous, polar, near circular orbit.
Data generated by ERS-1 mission contributes to;

- Improved understanding of ocean – atmosphere interactions
- Advances in knowledge of ocean circulation and energy transfer mechanisms
- Improved estimates of mass balance of the Arctic and Antarctic ice sheets
- Better monitoring of dynamic coastal processes
- Improved pollution monitoring
- Improved detection and land use changes

ERS-1 was launched on July 17, 1991 by Ariane 4 launcher from Kourou, French Guiana. ESA sponsored the mission. The prime contractor is Dornier (Germany). Co – contractors include Fokker (The Netherlands), Laben (Italy), Matra (France), McDonnel Detweiler Associates, Marconi (United Kingdom) and Selenia (Italy).
ERS-1 system characteristics are;

Operation frequency	: 5.25 GHz (C – band)
Wavelength	: 5.66 cm
Chirp bandwidth	:15.55 MHz
Pulse duration	:37.1 μsec
Pulse Repetition Frequency	:1680
Sampling frequency	:18.96 MHz
Quantization	:5 bits
Look angle	:23 degrees at midswath
Swath width	:100 km
Antenna length	:10 m

ERS-2

The ERS-2 satellite is essentially the same as ERS-1 except that it includes a number of enhancements and it is carrying a new payload instrument to measure the chemical composition of the atmosphere, named Global Ozone Monitoring Experiment (GOME). Through ERS-2, ESA intends to provide;

- The ability to map the Earth' s surface through clouds. Global wind and wave fields at high resolution.Global ocean dynamics and climatic instabilities. Identification of previously unidentified physical ocean features. Sea – surface manifestations of atmospheric phenomena.
- More accurate information about the polar regions: Topographic maps of polar ice sheets at an increased accuracy. Monitoring changes in ice sheets as indicators of climate change.
- Development of global and regional databases for use in climate modelling: Sea – surface temperature at increased accuracy. Sea – ice extent and concentration. Crop growth and desertification. Monitoring atmospheric aerosols.
- The ability to detect small changes in the Earth' s surface: Detection of landslides. Evolutions of volcanic eruptions. Detection of surface movement caused by earthquakes.

ERS-2 is carrying one completely new instrument compared to ERS-1: the Global Ozone Monitoring Experiment, GOME. This instrument provides spectra of backscattered sunlight in the ultra-violet / visible / near infrared part of the spectrum, while scanning a swath below the satellite. Processing of those spectra, in combination with direct solar spectra which are also measured by GOME for reference, allows the determination of concentrations and profiles of many trace gases, but particularly ozone, in the atmosphere.

ERS-2 was built by a consortium led by Deutsche Aerospace and was launced on April 20, 1995 on an Ariane. It has the same system characteristics as ERS-1.

APPENDIX B

Instantaneous Angular Frequency of a Chirp Pulse

A chirp pulse has;

$$g(t) = \exp[j.(wt - \phi(t))]$$

where

$$\phi(t) = -\frac{\alpha}{2}.t^2$$

At some time, t, call the total phase ϕ_0;

$$\phi_0 = w.t - \phi(t)$$

Exactly one period, T, later, the phase will increase to $\phi_0 + 2.\pi$;

$$w.(t+T) - \phi(t+T) = \phi_0 + 2.\pi$$

Thus, we have

$$w.T - [\phi(t+T) - \phi(t)] = 2.\pi$$

Dividing by T and recognizing that $2.\pi / T = w_{inst}$

$$w - [\phi(t+T) - \phi(t)]/T = 2.\pi / T = w_{inst}$$

However, T is very small, so $[\phi(t+T) - \phi(t)]/T$ is the derivative, $d\phi/dt$;

$$w - d\phi/dt = w_{inst}$$

As mentioned before;

$$\phi(t) = -\frac{\alpha}{2}.t^2$$

Hence;

$$\frac{d\phi}{dt} = -.\alpha.t$$

As a result;

$$w_{inst} = w + \alpha t$$

BIOGRAPHY

Cihan Erbaş was born in Istanbul in 1979. She began to study Electronics and Communication Engineering at Istanbul Technical University in 1997. She received her B.Sc. degree from the same university in 2001. She has been working at Electromagnetic Fields and Microwave Technique Division, Electronics and Communication Engineering Department, Istanbul Technical University as a research assistant since 2001.